Kinetic regulation of kinesin's two motor domains coordinates its stepping along microtubules

Yamato Niitani[1]‡, Kohei Matsuzaki[1,2]‡, Erik Jonsson[3], Ronald D. Vale[3] & Michio Tomishige[1,2]*

[1]Department of Applied Physics, School of Engineering, The University of Tokyo, Tokyo 113-8656, Japan, [2]Department of Physical Sciences, College of Science and Engineering, Aoyama Gakuin University, Sagamihara 252-5258, Japan, [3]Howard Hughes Medical Institute and Department of Cellular and Molecular Pharmacology, University of California, San Francisco, CA 94158, United States

‡ *These authors contributed equally to this work.*

*Correspondence should be addressed to: tomishige@phys.aoyama.ac.jp

ABSTRACT

The two identical motor domains (heads) of dimeric kinesin-1 move in a hand-over-hand process along a microtubule, coordinating their ATPase cycles such that each ATP hydrolysis is tightly coupled to a step and enabling the motor to take many steps without dissociating. The neck linker, a structural element that connects the two heads, has been shown to be essential for the head-head coordination; however, which kinetic step(s) in the chemomechanical cycle is "gated" by the neck linker remains unresolved. Here, we employed pre-steady state kinetics and single molecule assays to investigate how the neck linker conformation affects kinesin's motility cycle. We show that the backward-pointing configuration of the neck linker in the front kinesin head confers higher affinity for microtubules, but does not change ATP binding and dissociation rates. In contrast, the forward-pointing configuration of the neck linker in the rear kinesin head decreases the ATP dissociation rate but has little effect on microtubule dissociation. In combination, these conformation-specific effects of the neck linker favor ATP hydrolysis and dissociation of the rear head prior to microtubule detachment of the front head, thereby providing a kinetic explanation for the coordinated walking mechanism of dimeric kinesin.

INTRODUCTION

Kinesin-1 (hereafter called kinesin) is a dimeric motor protein that transports intracellular cargos by moving along microtubules. The unidirectional motion of kinesin toward the plus-end of the microtubule is driven by an N-terminal globular domain (termed "head") that catalyzes ATP hydrolysis and binds to the microtubule. The head is followed by a 14 amino-acid segment called the "neck linker" and then a long coiled-coil stalk that dimerizes the two identical polypeptide chains. Dimeric kinesin takes a 8 nm center-of-mass step by moving the rear head past the forward head along a microtubule protofilament once per ATP hydrolysis cycle; by alternating the movement of its two heads, kinesin can move processively for a micron or more without dissociating (Vale and Milligan, 2000; Asenjo et al., 2003; Kaseda et al., 2003; Asbury et al., 2003; Yildiz et al., 2004; Isojima et al., 2016; Wolff et al., 2023). The cycle of binding and dissociation of the head to/from the microtubule is tightly correlated with the ATPase cycle; release of ADP, creating a nucleotide-free state, stabilizes the microtubule binding of the head, while phosphate release after ATP hydrolysis induces detachment of the head from the microtubule (Gilbert and Johnson, 1994; Ma and Taylor, 1997a; Cross, 2004). Therefore, to alternately move the two heads, the ATP hydrolysis cycles in the rear and/or front heads should be differentially regulated ("gated"), such that the rear head hydrolyzes ATP and detaches from microtubule, prior to the front head (Hackney 1994; Ma and Taylor, 1997b; Gilbert et al., 1998; Auerbach and Johnson, 2005a; Cochran 2015).

To gate the ATPase cycles during processive movement, there must be a structural mechanism that enables the two heads to communicate with one another. When both heads are bound to the adjacent tubulin-binding sites ("two-head-bound state"), the front and rear heads are separated by 8 nm and cannot directly interact with each other. However, their neck linkers are highly extended and adopt two distinct configurations; the neck linker in the front head is stretched backward and the neck linker in the rear head is pointing forward, favoring the docked state (**Figure 1A;** Rice et al., 1999; Skiniotis et al., 2003; Tomishige et al., 2006; Liu et al., 2017). Artificially extending the neck linkers by inserting

polypeptide spacers reduces the coupling ratio between forward step and ATP turnover, indicating that the strain transmitted through the neck linkers has an essential role for the head-head coordination (Hackney et al., 2003; Yildiz et al., 2008; Shastry and Hancock, 2010; Andreasson et al., 2015; Isojima et al., 2016).

Several models, which are not mutually exclusive, have been put forth to explain the alternating catalysis of the two heads and high coupling between ATP turnover and stepping (Block, 2007; Valentine and Gilbert, 2007; Gennerich and Vale, 2009). One type of model proposes neck linker-based regulation of microtubule affinity. A “rear-head gating” version of this model proposes that forward strain posed through neck linker accelerates the detachment of the rear head. Evidence supporting this model is based on experiments showing that the two-headed kinesin hydrolyzes ATP and detaches from microtubule much faster than a one-headed kinesin (Hancock and Howard, 1999; Crevel et al., 2004; Schief et al., 2004), and that the detachment rate of the head from microtubule is faster under a forward than a rearward pulling force from an optical trap (Uemura et al., 2002). However, other experimental results showed that the detachment rate from the microtubule by the rear head of a dimer or of the monomer under assisting load was not significantly accelerated (Rosenfeld et al., 2003; Andreasson et al., 2015; Dogan et al., 2015).

Another class of gating models proposes that a chemical transition in the ATPase cycle is sensitive to neck linker tension between the two heads. A “front-head gating” model has been proposed that tension in the two-head bound state decreases ATP binding in the front head (Rosenfeld et al., 2003; Klumpp et al., 2004; Guydosh and Block, 2006; Dogan et al., 2015). Pre-steady state kinetic measurements showed that binding of mant-ATP (a fluorescent analogue that shows a signal change upon kinesin binding) to a microtubule-docked kinesin dimer showed single exponential kinetics with a signal amplitude nearly half than that expected if both heads can bind ATP (Rosenfeld et al., 2003; Klumpp et al., 2004). However, interpreting these results is complex, since the amplitude and duration of the mant-ATP signal is a composite from the front and rear heads, which complicates the

assignment of specific rate constants of nucleotide binding and unbinding or isomerization events to the two microtubule-bound heads.

In this study, we measured the ATP-binding and microtubule-detachment kinetics (**Figure 1B**) of the front and rear heads separately using pre-steady state and single-molecule measurements. To isolate and measure the kinetics of the front and rear head states separately, we utilized two methods: 1) disulfide-crosslinking to immobilize the neck linker in monomeric kinesin in the forward- or backward- pointing configurations (mimicking the rear and front head states, respectively), and 2) a heterodimeric kinesin in which one polypeptide chain was locked in neck linker -docked, rear head conformation. Our results provide quantitative evidence that both kinesin heads participate in a coordinated gating mechanism: the backward constraint of the neck linker in the front head reduces its detachment rate from microtubules without changing ATP on/off-rates, while the forward constraint on the neck linker in the rear head dramatically reduces ATP dissociation rate but has minimal effect on microtubule affinity. These results are consistent with the open and closed conformations of the nucleotide-binding pocket in the front and rear heads of microtubule-bound kinesin dimers observed in cryo-electron microscopy (cryo-EM) studies (Liu et al., 2017; Benoit et al., 2021) and provide a mechanism for the coordinated hand-over-hand movement of kinesin.

RESULTS

Controlling the neck-linker orientation of monomer kinesin through crosslinking

We first sought to examine the kinetics of nucleotide binding and microtubule dissociation of monomeric kinesin in which the neck linker was oriented either in the forward (mimicking the rear head) or the rearward (mimicking the front head) direction (**Figure 1A, C**). To control the orientation of the neck linker in monomer kinesin, we employed disulfide-crosslink between two cysteines, one on the head and the other on the neck linker (Tomishige and Vale, 2000). To immobilize the neck linker in this forward-pointing, docked conformation (Gigant et al., 2013), K222 (located at the plus-end oriented tip of the head) and E334 (the distal end of the docked neck linker) residues were substituted with cysteines in a Cys-light monomeric

kinesin (K339 Cys-light), whose solvent-exposed cysteines were replaced by either Ser or Ala (Rice et al., 1999) (**Figure 1C**, left). We refer to the C222/C334 crosslink here as "rear head crosslink". We previously introduced this cysteine pair into dimeric kinesin and found that oxidative crosslinking resulted in a complete loss of directionality (Tomishige and Vale, 2000). The neck linker of the front head is detached from the head, and its distal end is pulled backward (Skiniotis et al., 2003; Tomishige et al., 2006; Benoit et al., 2021). To constrain the neck linker in this backward-pointing configuration, which we refer to as the "front head crosslink", A47 (the minus-end-oriented base of the head) and T328 (five residues from the proximal end of the neck linker) residues were substituted with cysteines (**Figure 1C**, right). The cysteine pairs were covalently crosslinked by oxidative treatment with copper ion and o-phenanthroline (Kobashi, 1968; Kaan et al., 2011). The crosslinking efficiencies were estimated, by running SDS-PAGE under non-reducing conditions, to be 97% and 87% for the rear and front head crosslinks, respectively (**Figure 1D** and **Figure 1−figure supplement 1**).

We first evaluated the effect of disulfide crosslinking on the microtubule-activated ATP turnover rates (**Figure 1−figure supplement 2**). Under reducing conditions, the k_{cat} for both the rear and front head crosslinks (27.0 and 32.2 ATP/s per head, respectively) were lower than WT (57.1 ATP/s per head) (**Figure 1E**). The reduced ATPase activity primarily results from a decreased microtubule association rate (data to be presented elsewhere) with little change in ATP binding or microtubule dissociation rates (**Table 1**). For the rear head crosslink, the reduced ATPase activity might also be due to the presence of crosslinked species even under the reducing condition (~30%; **Figure 1D and Figure 1−figure supplement 1B**). Under oxidized conditions, the k_{cat} values for both rear and front head crosslinks were reduced by more than 10-fold compared to that under reducing condition (2.2 and 1.5 ATP/s per head, respectively (**Figure 1E** and **Table 1**)). These results demonstrate that neck linker constraints in both forward and rearward orientations inhibit specific steps in the mechanochemical cycle of the head.

155 **Effect of neck linker crosslinking on the binding/dissociation rates of ATP**
156 To measure ATP binding rate to kinesin head on the microtubule, we rapidly mixed the
157 nucleotide-free kinesin-microtubule complex with increasing concentrations of mant-ATP
158 using stopped flow apparatus. The initial rapid increase in the fluorescence represents mant-
159 ATP binding to the nucleotide pocket of the motor domain; this rapidly increasing phase was
160 fit with an exponential to obtain the observed rate k_{obs} (**Figure 2–figure supplement 1**). At
161 low mant-ATP concentrations, the k_{obs} increased linearly as a function of mant-ATP
162 concentration (Ma and Taylor, 1997a; Moyer et al., 1998); the slope of the fitted line provides
163 the binding rate k_{+1} and the offset provides the dissociation rate k_{-1} (**Figure 2A**). First, we
164 demonstrated that k_{+1} and k_{-1} of the wild-type head without Cys-modification were
165 unchanged after oxidization (**Table 1**) and were comparable to those previously reported
166 (Cross, 2004). Rear head crosslinking resulted in a modest decrease in the on-rate k_{+1} by
167 three-fold (5.1 and 1.6 $s^{-1}\mu M^{-1}$ under reducing and oxidizing conditions, respectively; **Figure**
168 **2B**). However, rear head crosslinking produced a 30-fold decrease in the off-rate k_{-1} (117 and
169 3.7 s^{-1} under reducing and oxidizing conditions, respectively). In contrast, front head
170 crosslinking resulted in only a modest and similar 2-fold decrease in both k_{+1} and k_{-1} (k_{+1} was
171 4.0 and 2.0 $s^{-1}\mu M^{-1}$, k_{-1} was 96 and 42 s^{-1} under reducing and oxidizing conditions,
172 respectively; **Figure 2B**), resulting in little or no change in the affinity for ATP after
173 crosslinking. These results indicate that the rear head crosslink reduces the ATP dissociation
174 rate, while the front head crosslink does not significantly alter the ATP binding kinetics. We
175 note that the measured k_{-1} of rear head crosslink was similar to the ATP turnover rate k_{cat}
176 (**Table 1**); therefore, it is likely that the majority of ATP molecules bound to the head were
177 hydrolyzed, and the observed fluorescence decrease rather represents mant-ADP release.
178
179 To detect the ATP dissociation event of the rear head, we employed a mutant kinesin with a
180 point mutation of E236A in the switch II loop, which almost abolishes ATPase hydrolysis
181 and traps in the microtubule-bound, neck-linker docked state (Rice et al., 1999; Auerbach
182 and Johnson, 2005b). The mant-ATP binding kinetics of E236A monomer revealed an ATP
183 on-rate (k_{+1} of 5.6 $s^{-1}\mu M^{-1}$) comparable to that of wild-type monomer (6.6 $s^{-1}\mu M^{-1}$), indicating

184 that the initial ATP-binding step remains unaffected by the mutation (**Figure 2C** and **Figure**
185 **2–figure supplement 2**). The ATP off-rate could not be precisely determined from the offset
186 value of the linear fitting of the k_{obs} plot due to its small magnitude.
187
188 To determine the ATP off-rate k_{-1} of E236A monomer, we employed single-molecule
189 fluorescence resonance energy transfer (smFRET) between the donor dye attached to the
190 head and the acceptor dye conjugated to ATP. The residue S55, separated by ~0.8 nm from
191 the nucleotide pocket, was substituted with cysteine and was labeled with ATTO488 or Cy3
192 dye; we would expect ~90% high FRET efficiency when Alexa 647-conjugated ATP (termed
193 as Alexa-ATP) binds to the labeled head (**Figure 2–figure supplement 4A**). Using wild-type
194 kinesin dimer, we demonstrated that Alexa-ATP acts as a substrate to drive kinesin motility
195 along microtubule, although velocities were about 10-fold lower than those driven by
196 unmodified ATP (**Figure 2–figure supplement 3**). First, we observed single-molecule FRET
197 of ATTO488-labeled "wild-type" monomer on microtubule in the presence of 500 nM Alexa-
198 ATP. We observed FRET efficiency increases upon Alexa-ATP binding to microtubule-bound
199 monomer, and then the donor and acceptor simultaneously disappeared (representing that the
200 head dissociated from microtubule after ATP hydrolysis; **Figure 2D**, left), or the donor
201 fluorescence recovered after disappearance of the acceptor fluorescence (representing that
202 ATP dissociated while the head remains bound to the microtubule; **Figure 2D**, right). We
203 found that the ATP bound to wild-type head could be either hydrolyzed, followed by head
204 dissociation from the microtubule, or reversibly dissociated with nearly equal probability
205 (**Figure 2D**). This finding is consistent with the mant-ATP binding kinetics measurements of
206 the monomer without neck-linker constraint, which showed similar k_2 and k_{-1} values (**Table**
207 **1**). In contrast, the single-molecule FRET observation of Cy3-labeled E236A monomer in
208 the presence of 200 nM Alexa-ATP showed that the majority of the Cy3-labeled mutant
209 remained bound to the microtubule during the observation period, and Alexa-ATP molecules
210 repeatedly bound and reversibly dissociated to/from the mutant head (**Figure 2E**). The mean
211 dwell time of the high FRET state (ATP-bound state) was 1.54 s, which corresponds to k_{-1} of
212 0.65 s^{-1} (**Figure 2F** and **Figure 2–figure supplement 4B**), a value 140-fold smaller than that

213 of the wild-type monomer (91 s^{-1}). We note that the neck linker of the E236A monomer was
214 neither pulled forward nor constrained by crosslinking; therefore, the ATP off-rate of
215 monomeric E236A may still be faster than that of the rear head in dimeric kinesin (as will be
216 examined later).
217
218 **Effect of neck linker crosslinking on the dissociation rate from microtubule**
219 Next, we analyzed the effect of the neck-linker crosslinking on the detachment rate of the
220 monomeric kinesin from microtubule (MT dissociation). First, we measured turbidity change
221 after rapidly mixing the nucleotide-free kinesin-microtubule complex with 1 mM ATP using
222 stopped-flow apparatus. Since monomeric kinesin repeatedly hydrolyzes ATP per encounter
223 to the microtubule through electrostatic interactions (Jiang and Hackney, 1997), we included
224 150 mM KCl to prevent reassociation of the detached head. However, the rear head crosslink
225 kinesin did not show any initial burst in turbidity after oxidative treatment (**Figure 3–figure**
226 **supplement 1**), because this constraint on the neck linker dramatically reduces the
227 microtubule-activated ADP release rate (data to be presented elsewhere), creating a weak
228 microtubule binding state. In contrast, the front head crosslink kinesin displayed an initial
229 burst phase for MT dissociation under these salt conditions. The fit of the initial decay
230 revealed a 7-fold decrease in the MT dissociation rate k_2 (51.5 and 7.0 s^{-1} for reduced and
231 oxidized conditions, respectively (**Figure 3A**)).
232
233 Since we could not measure the MT dissociation for the rear head using light scattering, we
234 sought an alternate approach involving visualizing GFP-fused K339 Cys-light kinesin
235 binding to the microtubule using single-molecule fluorescent microscopy in the presence of
236 100 mM KCl and 1 mM ATP (**Figure 3B**). The rear head crosslink showed a 6-fold reduced
237 binding frequency to microtubule (**Figure 3–figure supplement 2A**). We fit the histograms
238 of the dwell time of fluorescent spots on microtubule with single exponential decay (**Figure**
239 **3–figure supplement 2B**) and employed the inverse of the dwell time as a rough estimate of
240 the dissociation rate (termed as k_{2_SMF}). The k_{2_SMF} of the rear head crosslink was slightly
241 increased compared to before crosslinking (47.2 and 57.1 s^{-1} under reducing and oxidizing

242 conditions, respectively). In contrast, the front head crosslink showed an 18-fold decrease in
243 the k_{2_SMF} compared to before crosslinking (42.1 and 2.3 s^{-1} under reducing and oxidizing
244 conditions, respectively) (**Figure 3C** and **Table 1**). These results suggest that forward
245 constraint on the neck linker in the rear head does not significantly accelerate the detachment
246 from microtubule, while backward constraint of the neck linker in the front head reduces the
247 detachment rate.
248
249 **Different crosslinking schemes to examine the role of the neck-linker docking on gating**
250 The reduced detachment rate of the front head crosslink is likely due to the inability of the
251 C47/C328 crosslinked head to adopt the neck-linker docked conformation. Then, we asked
252 whether the reduced detachment rate can be recovered if the crosslinked neck linker is
253 allowed to partially dock onto the head. To test this, we crosslinked the neck linker in the
254 backward orientation between C47 on the head and C335 on the neck linker (**Figure 3D**,
255 right), which produces an extra 7 amino acids compared to C47/C328 between the base and
256 the crosslinked residues on the neck linker, allowing the initial few residues of the neck linker
257 (including I325 residue involved in filling the hydrophobic pocket exposed on the ATP-
258 bound head (Vale and Milligan, 2000; Sindelar, 2011; Cao et al., 2014)) to dock onto the head
259 (**Figure 3–figure supplement 3**). The ATP-induced detachment rate k_2 of C47/C335 showed
260 only two-fold reduction after crosslinking (41.6 and 19.4 s^{-1} for reduced and oxidized
261 conditions, respectively, measured using light scattering; **Figure 3A, C** and **Figure 3–figure**
262 **supplement 4C-E**). This finding is consistent with the idea that the gatekeeper of the front
263 head gate is the neck-linker docking and suggests that partial neck linker docking onto the
264 head is sufficient to half open the gate, while more extensive neck linker docking is required
265 to fully open the gate.
266
267 In contrast, the neck linker orientation in the rear head crosslink did not change the
268 dissociation rate from microtubules but reduced the dissociation rate of ATP (**Figure 2B**).
269 We examined an alternate crosslinking scheme between C4 on the N-terminal stretch and
270 C330 on the neck linker (Tomishige and Vale, 2000), which couples the neck linker (NL)

271 with the N-terminal flexible segment called "cover strand (CS)" (**Figure 3D**, left). The
272 interaction between the neck linker and cover strand has been shown to be important to
273 produce a forward-bias in the diffusional motion of the detached head against hindering load
274 (Hwang et al., 2008; Khalil et al., 2008). The ATP dissociation rate k_{-1} was not significantly
275 affected by C4/C330 crosslinking (148^{-1} and 96 s^{-1} for reduced and oxidized conditions,
276 respectively; **Figure 3E** and **Figure 3–figure supplement 4B**), indicating that the interaction
277 of the neck linker with the head, not with the N-terminal cover strand, is responsible for the
278 reduction of the ATP off-rate.
279
280 **A E236A-WT heterodimer to distinguish front and rear heads**
281 The front head crosslink was designed to constrain the neck linker to mimic the neck linker
282 orientation of the front head. However, it differs from that of the front head in that the
283 backward-pointing configuration is maintained by the crosslinking, not by the backward
284 strain originating from the stretched neck linkers between two microtubule-bound heads
285 (Hyeon and Onuchic, 2007; Hariharan and Hancock, 2009). We sought to further investigate
286 how the neck linker tension contributes to the front head gating by examining the nucleotide-
287 binding and microtubule detachment kinetics of the front head in the context of a dimeric
288 kinesin. To this end, we employed a heterodimer in which one polypeptide is wild-type (WT)
289 and the other contains the E236A mutation (E236A-WT heterodimer). As described above,
290 E236A mutant acts as a long-lived rear head, which is kinetically trapped in the neck-linker
291 docked, pre-ATP hydrolysis state. Thus, in the E236A-WT heterodimer in the presence of
292 ATP, one would expect the E236A head to be in the rear and the WT head to occupy the front.
293
294 To test this assumption, we used the smFRET sensor, which has been used to distinguish the
295 configurations of two heads (Mori et al., 2007). We first introduced one cysteine into the
296 residue 215 (located at the plus-end oriented tip of the head) of the E236A chain and another
297 into the residue 43 (located at the minus-end oriented base of the head) of WT chain and
298 labeled with Cy3 and Cy5 fluorophores (**Figure 4–figure supplement 1**, left). The FRET
299 efficiency of dual-labeled molecules bound to the microtubule in the presence of ATP showed

300 a single peak at about 90%. When we introduced 43Cys into the E236A chain and 215Cys
301 into the WT chain, however, the distribution of the FRET efficiency showed a single peak at
302 about 10% (**Figure 4–figure supplement 1**, right). These results are consistent with E236A-
303 WT heterodimer stably taking two-head-bound state, in which WT head is in the front and
304 E236A head is in the rear position.
305
306 **ATP binding kinetics of the front and rear heads of the heterodimer**
307 First, we measured the steady-state microtubule-activated ATPase activity of the E236A-WT
308 heterodimer. The microtubule-activated ATPase k_{cat} of the E236A-WT heterodimer was 4.6
309 ATP/s per head (**Figure 6–figure supplement 1**), suggesting that the front WT head is
310 capable of hydrolyzing ATP, but its catalytic activity is suppressed (c.f. ~30 ATP/s per head
311 for wild-type dimer (Tomishige and Vale, 2000)). As described later, the reduced ATPase rate
312 results from suppressed microtubule detachment of the front WT head, while the rear E236A
313 head is virtually unable to detach from microtubules.
314
315 Next, we measured ATP-binding kinetics of the wild-type front head in the E236A-WT
316 heterodimer using a stopped-flow apparatus. To selectively observe fluorescent signal of
317 mant-ATP bound to the wild-type front head, we quenched the fluorescent signal of mant-
318 ATP bound to the E236A head by substituting residue H100 (located in loop 5 near the
319 nucleotide pocket) in the E236A chain with cysteine and labeling it with Alexa 488 dye,
320 which acts as an acceptor for mant-ATP (**Figure 4A**, upper). The measured ATP on-rate k_{+1}
321 and off-rate k_{-1} were 5.3 $\mu M^{-1}s^{-1}$ and 92 s^{-1}, respectively (**Figure 4B, C, F** and **Figure**
322 **4–figure supplement 2**), which were similar to those of the un-crosslinked monomer
323 (**Figure 2C, F**). These results further support the notion that ATP binding kinetics of the front
324 head are not significantly affected by the backward strain posed to the neck linker.
325
326 We also measured ATP-binding kinetics of the E236A rear head of the heterodimer. Pre-
327 steady state kinetic measurements using E236A-WT heterodimer with Alexa 488
328 modification on the wild-type head (**Figure 4A**, lower) revealed an ATP on-rate k_{+1} of 4.4

329 $\mu M^{-1}s^{-1}$ (**Figure 4B, C** and **Figure 4–figure supplement 2**), similar to that of un-crosslinked
330 WT and E236A monomers (**Figure 2C**). Since the ATP off-rate k_{-1} could not be accurately
331 measured using stopped-flow (k_{-1} was $-3.3\ s^{-1}$), we used smFRET between a donor Cy3 on
332 the E236A rear head (with cysteine modification at S43) and an acceptor Alexa-ATP. We
333 expected ~80% high FRET when Alexa-ATP bound to the rear E236A head (dye distance
334 ~2.5 nm; **Figure 4D**, upper) and low FRET when ATP bound to the front wild-type head (dye
335 distance ~9 nm; **Figure 4D**, lower). The high FRET state showed a mean dwell time of 65.5
336 s, corresponding to k_{-1} of 0.015 s^{-1} (**Figure 4E, F** and **Figure 4–figure supplement 3**). This
337 ATP off-rate is 42-fold smaller than that of the E236A monomer (**Figure 2E, F**), indicating
338 that forward strain prevents nucleotide release.
339
340 **Microtubule detachment rate of the front head of E236A-WT heterodimer**
341 Next, we measured ATP-induced detachment rate k_2 of the front WT head of E236A-WT
342 heterodimer from the microtubule using high-speed single-molecule microscopy (**Figure 5A**;
343 Isojima et al., 2016). We labeled WT head with a gold nanoparticle (40 nm in diameter) and
344 observed the motion of the gold probe attached to E236A-WT heterodimer on the
345 microtubule in the presence of 1 mM ATP. With the temporal resolution of the measurement
346 (50 μs), we could clearly identify transient increases in the fluctuation of the gold probe
347 accompanied by detachment of the labeled head (**Figure 5B**). Moreover, these observations
348 allowed us to distinguish whether the gold-labeled WT head was in the leading or trailing
349 position just before microtubule detachment; the backward displacement of the detached
350 head indicates that the labeled WT head occupied the leading position prior to detachment
351 (**Figure 5–figure supplement 1**). Unlike the unbound trailing head of wild-type dimer that
352 showed continuous mobility (Isojima et al., 2016), the unbound WT head of E236A-WT
353 heterodimer exhibited a low-fluctuation state in the middle (**Figure 5B,** s.d. traces). This low-
354 fluctuation unbound state was distinguishable from the typical microtubule-bound state,
355 having a shorter dwell time of ~5 ms compared to the bound state and positioning backward,
356 closer to the E236A head, relative to the bound state (**Figure 5–figure supplement 2**). The

357 mean dwell time of the bound and unbound states of the front head at 1 mM ATP was 160
358 and 11 ms, respectively (**Figure 5C** and **Figure 5–figure supplement 3**).
359
360 To determine the rate constants for the ATP-promoted detachment rate of the front WT head,
361 we measured the dwell time of microtubule-bound state of the gold-labeled WT head under
362 various ATP conditions (**Figure 5D** and **Figure 5–figure supplement 3**). The mean dwell
363 time increased as ATP concentration was decreased (**Figure 5E**), indicating that the bound
364 dwell time includes ATP-binding and hydrolysis in the front head. The inverse of the mean
365 dwell time plotted against ATP concentration could be well fit with a Michaelis-Menten
366 equation with fit parameters of k_{cat} = 6.3 ± 0.2 s^{-1} and K_m = 43 ± 6 μM (**Figure 6D**). The
367 observed k_{cat} also includes ADP release rate; however, since ADP release (~5 ms) becomes
368 negligible within the dwell time of >160 ms, we took this k_{cat} as an approximation of the
369 ATP-promoted detachment rate k_2. The k_2 determined using E236A-WT heterodimer (6.3 s^{-}
370 ^{1}) is similar to the k_2 of front head crosslink (7.0 s^{-1}), supporting the notion that the backward
371 strain posed to the neck linker significantly reduces nucleotide-induced detachment rate of
372 the front head. In contrast, the dwell time of the unbound state of the gold-labeled WT head
373 showed weak ATP dependence (**Figure 5–figure supplement 2**), indicating that the rear
374 E236A head occasionally releases ATP when the front head detaches from the microtubule
375 and the neck linker of E236A head becomes unconstrainted. This finding further supports the
376 idea that forward neck linker strain plays a crucial role in reducing the reversible ATP release
377 rate.
378
379 **Effect of the neck-linker tension on the gating of the front and rear heads**
380 Experimental results obtained from neck-linker crosslinking monomers and the E236A-WT
381 heterodimer revealed that distinct chemical steps are gated in the front and rear heads (k_2 and
382 k_{-1} respectively). We next sought to examine whether neck linker tension places a role in
383 gating these steps. To reduce the tension posed to the neck linker in the two-head-bound state,
384 we extended the neck linker of E236A-WT heterodimer by inserting 7 or 12 glycine residues
385 between neck linker and neck coiled-coil of both chains (referred to as G7 and G12) (**Figure**

386 **6A**; Isojima et al., 2016). The microtubule-activated ATPase rate of G12 increased modestly
387 by 1.6-fold compared to that of the heterodimer without neck-linker extension (referred to as
388 G0) (**Figure 6B and Figure 6–figure supplement 1**).
389
390 We first examined the effect of the tension posed to the neck linker on ATP-induced
391 detachment rate k_2 of the front head, by observing the neck-linker extended E236A-WT
392 heterodimer using high-speed dark-field microscopy. The gold probe attached to the front
393 WT head of G7 and G12 heterodimers showed transient increases in the fluctuation of the
394 gold probe (**Figure 6C**). The inverse of the dwell time of bound state for G7 and G12 mutants
395 (**Figure 6–figure supplement 2, 3**) plotted against ATP concentration fit well with the
396 Michaelis-Menten equation (**Figure 6D**); the fit parameters are k_{cat} = 7.6 ± 0.9 s^{-1} and K_m =
397 22 ± 10 μM for G7 and k_{cat} = 9.3 ± 0.7 s^{-1} and K_m = 6.1 ± 2.1 μM for G12. The k_2 modestly
398 increased as the inserted poly-Gly number increased; G12 showed 1.5-fold increase in k_2
399 compared to G0 (**Figure 6E**), reminiscent of the results of ATPase rates (**Figure 6B**). The
400 detached WT head of G12 heterodimer occasionally bound to the rear-tubulin binding site
401 (the frequency was 14% among all binding events); however, the head detached from the
402 rear-binding position much faster (19 ms at 1 mM ATP; **Figure 6–figure supplement 4**) than
403 from the front-binding site (111 ms), indicating that the orientation of the neck linker has
404 greater effect on the front head gating than the tension. These findings demonstrate that the
405 detachment rate of the front head is not greatly affected by the amount of tension posed to
406 the neck linker, at least within the range of 12 glycine insertions.
407
408 Next, we examined the effect of the tension posed to the neck linker on ATP off-rate k_{-1} of
409 the rear E236A head of the E236A-WT heterodimer, by measuring smFRET between Cy3-
410 labeled E236A head and Alexa-ATP. When compared to the heterodimer without neck linker
411 extension (0.015 s^{-1}; **Figure 4E**), k_{-1} determined from the inverse of the mean dwell time of
412 the high FRET state only modestly increased for G7 (0.018 s^{-1}) and increased by 5-fold for
413 G12 (0.081 s^{-1}) (**Figure 6F** and **Figure 6–figure supplement 5**). The k_{-1} was further
414 increased for monomeric E236A without neck linker constraint as described before (0.65 s^{-1};

415 **Figure 2F and 6F**). These results indicate that the ATP off-rate of the rear E236A head is
416 significantly affected by the amount of the forward strain, especially when the neck linker
417 was extended with more than 7 glycine insertions.
418
419 **DISCUSSION**
420 To identify the chemical transition that is gated in the front and/or rear head, we measured
421 ATP binding and microtubule detachment kinetics of kinesin's catalytic domain with neck
422 linker constraints imposed by 1) disulfide crosslinking of the neck linker in monomeric
423 kinesin in backward (rear head -like) and forward (front head -like) orientations, and 2) using
424 the E236A-WT heterodimer to create a two-head microtubule-bound state with the mutant
425 and WT heads occupying the rear and front positions respectively. As also described in the
426 Results, these two experimental paradigms each have their unique caveats in terms of how
427 faithfully they replicate a native moving kinesin dimer. We also used potentially perturbing
428 measurement approaches that involve using fluorescently-labeled ATP or modifying
429 cysteine-lite kinesin with fluorescent dyes or gold particles. However, the results from these
430 two different experimental approaches and the variety of different measurements approaches
431 all yielded consistent results, which are summarized below.
432
433 In the front head, backward orientation of the neck linker has little effect on ATP binding
434 and dissociation rates, both when measured for a monomer crosslink (**Figure 2A, B**) and
435 for the front head of a E236A-WT heterodimer (**Figure 4B, C, F**). These findings differ
436 from a prevailing view that the ATP-binding step is gated in the front head (Rosenfeld et al.,
437 2003; Klumpp et al., 2004; Guydosh and Block, 2006; Dogan et al., 2015). However, we
438 found that the ATP-induced detachment rates from microtubule (k_2) were similarly reduced
439 for both the front head crosslink (7.0 s^{-1}; **Figure 3A**) and the front WT head of the
440 E236A/WT heterodimer (6.3 s^{-1}; **Figures 6D**), suggesting that a step subsequent to ATP
441 binding is gated in the front head. These results are consistent with an inability of the front
442 head to fully close its nucleotide pocket to promote ATP hydrolysis and Pi release (Benoit
443 et al., 2023), as will be discussed later.

444

445 We also provide evidence for a rear-head gating mechanism that involves a tighter affinity
446 for ATP (due to a decrease in reversible ATP-dissociation rate k_{-1}) without a change in
447 microtubule affinity in the ATP-bound state. The K_d of ATP for the front head crosslink and
448 the monomer without constraint are similar (~20 μM), and substantially higher than our
449 estimated 4 nM K_d of ATP for the rear E236A head of the E236A-WT heterodimer. We note,
450 however, that this K_d of ATP may somewhat underestimate the true value in wild-type kinesin
451 for two reasons: first, the E236A mutation likely stabilizes the neck linker-docked, closed
452 state more than in the rear head of the wild-type dimer (Rice et al., 1999), and second, the
453 Alexa-ATP used to measure the ATP off-rate of E236A head showed ~10-fold smaller
454 velocity compared to unmodified ATP, partly due to a slower ATP off-rate (**Figure 2–figure**
455 **supplement 3**). While these caveats may diminish the observed 5000-fold difference in the
456 K_d of ATP in native kinesin, these results nevertheless point to large difference in ATP affinity
457 between the front and rear heads. The difference in the ATP-affinity between the front and
458 rear heads can explain previous experimental results supporting the front-head gating
459 mechanism (Uemura and Ishiwata, 2003; Rosenfeld et al., 2003; Klumpp et al., 2004;
460 Guydosh and Block, 2006; Dogan et al., 2015), although our direct kinetic measurements
461 show that this difference is manifest through in a stronger affinity for ATP in the rear head
462 rather than a weaker affinity in the front head. While the neck linker position of the rear head
463 increases the affinity of bound ATP, it does not significantly accelerate k_2, which includes the
464 ATP hydrolysis and Pi release steps in the chemical cycle.

465

466 **Kinetic gating aids head-head coordination but does not prevent progression through**
467 **the ATPase cycle**

468 Our results show that the front head gate slows down but does not block its ATPase cycle.
469 The ATP-induced microtubule detachment rate k_2 of the front head is 6-7 s^{-1} (7.0 s^{-1} for the
470 front head monomer crosslink and 6.3 s^{-1} for the front head of E236A-WT heterodimer)
471 which is similar to its overall ATPase rate (4.6 s^{-1}). These rate constants are sufficiently low
472 to keep the catalytic cycles of two heads largely out of phase, since the detachment rate of

473 the rear head of wild-type dimer (inverse of the dwell time from two-head-bound state to
474 one-head-bound state during processive movement) is ~100 s^{-1} (Isojima et al., 2016). The
475 observed detachment of the front head of E236A-WT heterodimer is likely caused by ATP
476 hydrolysis of the front head, because 1) ATP turnover rate of this heterodimer was similar to
477 the k_2 value, and 2) the dwell time of the bound state of the front head on microtubule was
478 dependent on the ATP concentration. These results suggest that the kinesin's head can slowly
479 hydrolyze ATP and detach from microtubule without the aid of neck-linker docking. This
480 idea can explain how kinesin dimer takes repetitive back steps under large hindering loads.
481 Carter and Cross (2005) showed that kinesin takes 8-nm backward steps at supra-stall forces
482 (>7 pN) exerted using an optical trap, and that the stepping rate was dependent on the ATP
483 concentration (~0.3 steps/s and ~1 step/s at 1 mM and 10 μM ATP conditions, respectively),
484 which are comparable to the dwell times that we found for the microtubule-bound state of
485 the front head of E236A-WT heterodimer (0.16 s and 1.1 s at 1 mM and 10 μM ATP,
486 respectively; **Figure 5–figure supplement 3**). These results suggest that the back steps are
487 likely caused by the neck-linker docking-independent slow ATP catalysis of the front head
488 followed by its dissociation from the microtubule in an ADP-bound state.
489
490 **A kinetic and structural model for kinesin gating**
491 The difference in the ATP binding affinity between the front (low affinity) and rear (high
492 affinity) heads suggests a structural difference in their nucleotide binding pockets. Indeed,
493 the high ATP affinity state of the neck linker -docked rear head is consistent with a "closed"
494 nucleotide pocket observed in crystal and cryo-EM structures of kinesin-1 bound to tubulin
495 and complexed with a non-hydrolyzable ATP analog in kinesin's active site (Shang et al.,
496 2005; Gigant et al., 2013). Moreover, a recent high-resolution cryo-EM image of the
497 microtubule-bound KIF14 dimer showed that while they could observe nucleotide in the
498 active site of the front head, the structure of the pocket was more "open" and similar to that
499 of a nucleotide-free head (Shang et al., 2014; Cao et al., 2014; Benoit et al., 2021). Since the
500 switch I and II loops that are involved in hydrolysis reaction are positioned away from the γ-
501 phosphate in the opened nucleotide pocket, the open state is incompatible with ATP

hydrolysis, while the closed state is competent in ATP hydrolysis (Kull and Endow, 2002; Parke et al., 2010) (**Figure 7–figure supplement 1B**). Thus, these structural features are consistent with our kinetics results.

These findings suggest that the isomerization from the open to closed conformational state, rather than the chemical transition, is gated by the neck linker constraint (**Figure 7–figure supplement 2**). This aligns with our structural modeling of kinesin dimer in the two-head-bound state (Makino et al., 2024), which showed that conformational transitions are suppressed for both the front head (from open to closed state) and the rear head (from closed to open state), as these changes would cause an intolerable increase in tension on the disordered neck linker region (**Figure 7**). We demonstrated, using the loose C47/C335 backward crosslink of the neck linker, that neck linker docking is responsible for opening the gate (i.e., the open to closed transition) (**Figure 3A-D**). The C47/C335 crosslink forms a short 7-amino acid flexible loop, which is insufficient for the formation of two β-sheets (residues 326-334) (**Figure 3–figure supplement 3**). However, it allows the conformational transition of the initial segment of the neck linker (residues 323-325); K323 and T324 residues form an α-helix extending the C-terminus of α6, while the I325 residue plays a particularly important role in docking onto the hydrophobic pocket exposed on the closed head. Given that the hydrophobic pocket is positioned forward from the neck linker's base (**Figure 7–figure supplement 1A**), the docking of the I325 side chain is suppressed in the front head, as it would cause an intolerable increase in tension (entropy decrease) on the disordered neck linker (Makino et al., 2024), thus maintaining the open state. The neck linker extension had a smaller effect on front-head gating (**Figure 6E**), likely because a stable interaction between the I325 side chain and the hydrophobic pocket is necessary to maintain the closed state until ATP hydrolysis completes. In contrast, the neck linker extension had a larger effect on the rear head's ATP affinity (**Figure 6F**). This is probably because the rear head can occasionally transition back to an open state (followed by reversible ATP release) without tension on the neck linker (**Figure 2D**; Rice et al., 2003). Thus, forward strain plays a crucial role in aiding I325 residue docking and stabilizing the closed state.

In summary, our findings, together with structural data discussed above, are consistent with an asynchronous sequence of events in the front and rear kinesin heads that help to coordinate their chemomechanical cycles to ensure their continuous stepping along the microtubule (**Figure 7**). In the rear head, ATP binding is followed rapidly by an isomerization step that closes the nucleotide pocket, decreasing the rate of nucleotide dissociation and facilitating ATP hydrolysis. This conformational change is facilitated by docking of the neck linker in its forward orientation (Benoit et al., 2003). In the front head, in contrast, the backward conformation of neck linker favors an open nucleotide pocket, which helps to prevent the microtubule-bound front head from proceeding with ATP hydrolysis before the rear head detaches. Once the rear head detaches, the front head "gate" is relieved, allowing the neck linker to dock and its nucleotide pocket to close. This asynchrony in the timing of ATP hydrolysis minimizes the likelihood of both heads simultaneously entering an ADP-state and dissociating from microtubule. Recent cryo-EM studies and modeling of the kinesin dimer under various nucleotide states support the proposal that the open-closed conformational transition is gated by the neck linker strain; however, direct evidence for this conformational transition in the context of a processively moving kinesin dimer would help to further substantiate this model.

Acknowledgments

We thank M. Nakajima and Y. Sakai for support with cloning. M.T. was supported by MEXT KAKENHI Grant Number 17H03661 and by JSPS KAKENHI Grant Numbers JP20H05542, JP22H04850.

Author contributions

Yamato Niitani, Conceptualization, Investigation, Formal analysis, Software, Methodology, Visualization; Kohei Matsuzaki, Investigation, Formal analysis, Software, Methodology, Visualization; Erik Jonsson, Investigation, Formal analysis, Methodology; Ronald Vale, Methodology, Supervision, Funding acquisition, Writing – review and editing; Michio

Tomishige, Conceptualization, Methodology, Supervision, Funding acquisition, Writing – original draft, Project administration, Writing - review and editing

564 **REFERENCES**

565 Aitken, C. E., Marshall, R. A. & Puglisi, J. D. An oxygen scavenging system for
566 improvement of dye stability in single-molecule fluorescence experiments. *Biophys. J.*
567 **94**, 1826–1835 (2008).
568 Andreasson, J. O. L. *et al.* Examining kinesin processivity within a general gating
569 framework. *eLife* 2015;4:e07403.
570 Asbury, C. L., Fehr, A. N. & Block, S. M. Kinesin moves by an asymmetric hand-over-
571 hand mechanism. *Science* **302**, 2130-2134 (2003).
572 Asenjo, A. B., Krohn, N. & Sosa, H. Configuration of the two kinesin motor domains
573 during ATP hydrolysis. *Nature Struct. Biol.* **10**, 836-842 (2003).
574 Auerbach, S. D. & Johnson, K. A. Alternating site ATPase pathway of rat conventional
575 kinesin. *J. Biol. Chem.* **280**, 37048-37060 (2005a).
576 Auerbach, S. D. & Johnson, K. A. Kinetic effects of kinesin switch I and switch II mutants.
577 *J. Biol. Chem.* **280**, 37061-37068 (2005b).
578 Benoit M. P. M. H. *et al*. Structural basis of mechano-chemical coupling by the mitotic
579 kinesin KIF14. *Nat. Commun.* **12**, 3637 (2021).
580 Benoit, M. P. M. H., Hunter, B., Allingham, J. S. & Sosa, H. New insights into the
581 mechanochemical coupling mechanism of kinesin-microtubule complexes from their
582 high-resolution structures. *Biochem. Soc. Trans.* **51**, 1505-1520 (2023).
583 Block, S. M. Kinesin motor mechanics: binding, stepping, tracking, gating, and limping.
584 *Biophys. J.* **92**, 2986-2995 (2007).
585 Cao, L. *et al*. The structure of apo-kinesin bound to tubulin links the nucleotide cycle to
586 movement. *Nat. Commun.* **5**, 5364 (2014).
587 Carter, N. J. & Cross, R. A. Mechanics of the kinesin step. *Nature* **435**, 308-312 (2005).
588 Cochran, J. C. Kinesin motor enzymology: chemistry, structure, and physics of nanoscale
589 molecular machines. *Biophys. Rev.* **7**, 269-299 (2015).
590 Crevel, I. M.-T. *et al*. What kinesin does at roadblocks: the coordination mechanism for
591 molecular walking. *EMBO J.* **23**, 23-32 (2004).
592 Cross, R. A. The kinetic mechanism of kinesin. *Trends Biochem. Sci.* **29**, 301-309 (2004).

593 Denoncin, K., Nicolaes, V., Cho, S.-H., Leverrier, P. & Collet, J.-F. Protein disulfide bond
594 formation in the periplasm: determination of the in vivo redox state of cysteine residues.
595 *Methods Mol. Biol.* **966**, 325-336 (2013).
596 Dogan, M. Y., Can, S., Cleart, F. B., Purde, V. & Yildiz, A. Kinesin's front head is gated by
597 the backward orientation of its neck linker. *Cell Rep.* **10**, 1967-1973 (2015).
598 Gennerich, A. & Vale, R. D. Walking the walk: how kinesin and dynein coordinate their
599 steps. *Curr. Opin. Cell Biol.* **21**, 59-67 (2009).
600 Gigant, B. *et al*. Structure of a kinesin–tubulin complex and implications for kinesin
601 motility. *Nat. Struct. Mol. Biol*. **20**, 1001–1007 (2013).
602 Gilbert, S. P. & Johnson, K. A. Pre-steady-state kinetics of the microtubule-kinesin
603 ATPase. *Biochemistry* **33**, 1951-1960 (1994).
604 Gilbert, S. P., Moyer, M. L. & Johnson, K. A. Alternating site mechanism of the kinesin
605 ATPase. *Biochemistry* **37**, 792-799 (1998).
606 Guydosh, N. R. & Block, S. M. Backsteps induced by nucleotide analogs suggest the front
607 head of kinesin is gated by strain. *Proc. Natl. Acad. Sci. USA* **103**, 8054-8059 (2006).
608 Hackney, D. D. Evidence for alternating head catalysis by kinesin during microtubule-
609 stimulated ATP hydrolysis. *Proc. Natl. Acad. Sci. USA* **91**, 6865-6869 (1994).
610 Hackney, D. D., Stock, M. F., Moore, J. & Patterson, R. A. Modulation of kinesin half-site
611 ADP release and kinetic processivity by a spacer between the head groups. *Biochemistry*
612 **42**, 12011-12018 (2003).
613 Hancock, W. O. & Howard, J. Kinesin's processivity results from mechanical and chemical
614 coordination between the ATP hydrolysis cycles of the two motor domains. *Proc. Natl.*
615 *Acad. Sci. USA* **96**, 13147-13152 (1999).
616 Hariharan, V. & Hancock, W. O. Insights into the mechanical properties of the kinesin neck
617 linker domain from sequence analysis and molecular dynamics dimulations. *Cel Mol*
618 *Bioeng* **2**, 177–189 (2009).
619 Hwang, W., Lang, M. J. & Karplus, M. Force generation in kinesin hinges on cover-neck
620 bundle formation. *Structure* **16**, 62-71 (2008).

621 Hyeon, C. & Onuchic, J. N. Internal strain regulates the nucleotide binding site of the
622 kinesin leading head. *Proc. Natl. Acad. Sci. USA* **104**, 2175-2180 (2007).
623 Isojima, H., Iino, R., Niitani, Y., Noji, H. & Tomishige, M. Direct observation of
624 intermediate states during the stepping motion of kinesin-1. *Nature Chem. Biol*. **12**, 290-
625 297 (2016).
626 Jiang, W. & Hackney, D. D. Monomeric kinesin head domains hydrolyze multiple ATP
627 molecules before release from a microtubule. *J. Biol. Chem.* **272**, 5616–5621 (1997).
628 Kaan, H. Y. K., Hackney, D. D. & Kozielski, F. The structure of the kinesin-1 motor-tail
629 complex reveals the mechanism of autoinhibition. *Science* **333**, 883-885 (2011).
630 Kaseda, K., Higuchi, H. & Hirose, K. Alternate fast and slow stepping of a heterodimeric
631 kinesin molecule. *Nature Cell Biol.* **5**, 1079-1082 (2003).
632 Klumpp, L. M., Hoenger, A. & Gilbert, S. P. Kinesin's second step. *Proc. Natl. Acad. Sci.*
633 *USA* **101**, 3444-3449 (2004).
634 Khalil, A. S. *et al.* Kinesin's cover-neck bundle folds forward to generate force. *Proc. Natl.*
635 *Acad. Sci. USA* **105**, 19247-19252 (2008).
636 Kobashi, K. Catalytic oxidation of sulfhydryl groups by *o*-phenanthroline copper complex.
637 *Biochim. Biophys. Acta* **158**, 239-245 (1968).
638 Kull, F. J. & Endow, S. A. Kinesin: switch I & II and the motor mechanism. *J. Cell Sci.*
639 **115**, 15-23 (2002).
640 Liu, D., Liu, X., Shang, Z. & Sindelar, C. V. Structural basis of cooperativity in kinesin
641 revealed by 3D reconstruction of a two-head-bound state on microtubule. *eLife*
642 2017;6:e24490.
643 Ma, Y.-Z. & Taylor, E. W. Kinetic mechanism of a monomeric kinesin construct. *J. Biol.*
644 *Chem.* **272**, 717-723 (1997a).
645 Ma, Y.-Z. & Taylor, E. W. Interacting head mechanism of microtubule-kinesin ATPase. *J.*
646 *Biol. Chem.* **272**, 724-730 (1997b).
647 Makino, T. *et al.* Tension-induced suppression of allosteric conformational changes
648 explains coordinated stepping of kinesin-1. bioRxiv ?? (2024).

649 Mori, T., Vale, R. D. & Tomishige, M. How kinesin waits between steps. *Nature* **450**, 750-
650 754 (2007).
651 Moyer, M. L., Gilbert, S. P. & Johnson, K. A. Pathway of ATP hydrolysis by monomeric
652 and dimeric kinesin. *Biochemistry* **37**, 800–813 (1998).
653 Parke, C. L., Wojcik, E. J., Kim, S. & Worthylake, D. K. ATP hydrolysis in Eg5 kinesin
654 involves a catalytic two-water mechanism. *J. Biol. Chem.* **285**, 5859-5867 (2010).
655 Rice, S. *et al*. A structural change in the kinesin motor protein that drives motility. *Nature*
656 **402**, 778-784 (1999).
657 Rice S. *et al.* Thermodynamic properties of the kinesin neck-region docking to the catalytic
658 core. *Biophys. J.* **84**, 1844-1854 (2003).
659 Rosenfeld, S. S. *et al*. Stepping and stretching: how kinesin uses internal strain to walk
660 processivity. *J. Biol. Chem.* **278**, 18550-18556 (2003).
661 Schief, W. R., Clark, R. H., Crevenna, A. H. & Howard, J. Inhibition of kinesin motility by
662 ADP and phosphate supports a hand-over-hand mechanism. *Proc. Natl. Acad. Sci. USA*
663 **101**, 1183-1188 (2004).
664 Shang, Z. *et al.* High-resolution structures of kinesin on microtubules provide a basis for
665 nucleotide-gated force-generation. *eLife* 2014;3:e04686.
666 Shastry, S. & Hancock, W. O. Neck linker length determines the degree of processivity in
667 kinesin-1 and kinesin-2 motors. *Curr. Biol.* **20**, 939-943 (2010).
668 Sindelar, C. V. A seesaw model for intermolecular gating in the kinesin motor protein.
669 *Biophys. Rev.* **3**, 85-100 (2011).
670 Skiniotis, G. *et al*. Nucleotide-induced conformations in the neck region of dimeric kinesin.
671 *EMBO J.* **22**, 1518-1528 (2003).
672 Tomishige, M. & Vale, R. D. Controlling kinesin by reversible disulfide cross-linking:
673 identifying the motility-producing conformational change. *J. Cell Biol.* **151**, 1081-1092
674 (2000).
675 Tomishige, M., Stuurman, N. & Vale, R. D. Single-molecule observations of neck linker
676 conformational changes in the kinesin motor protein. *Nature Struct. Mol. Biol.* **13**, 887-
677 894 (2006).

678 Uemura, S. *et al.* Kinesin-microtubule binding depends on both nucleotide state and
679 loading direction. *Proc. Natl. Acad. Sci. USA* **99**, 5977-5981 (2002).
680 Uemura, S. & Ishiwata, S. Loading direction regulates the affinity of ADP for kinesin.
681 *Nature Struct. Biol.* **10**, 308-311 (2003).
682 Vale, R. D. & Milligan R. A. The way things move: looking under the hood of molecular
683 motor proteins. *Science* **288**, 88-95 (2000).
684 Valentine, M. T. & Gilbert, S. P. To step or not to step? How biochemistry and mechanics
685 influence processivity in kinesin and Eg5. *Curr. Opin. Cell Biol.* **19**, 75-81 (2007).
686 Wolff, J. O. *et al*. MINFLUX dissects the unimpeded walking of kinesin-1. *Science* **379**,
687 1004-1010 (2023).
688 Yildiz, A., Tomishige, M., Vale, R. D. & Selvin, P. R. Kinesin walks hand-over-hand.
689 *Science* **303**, 676-678 (2004).
690 Yildiz, A., Tomishige, M., Gennerich, A. & Vale, R. D. Intramolecular strain coordinates
691 kinesin stepping behavior along microtubules. *Cell* **134**, 1030-1041 (2008).
692
693

694 ## Materials and methods

695 **DNA cloning and protein purification**

696 We used a 339 amino-acid "cysteine-light" mutant or a 349 amino-acid wild-type human
697 kinesin-1 monomer as a template for mutagenesis. Cysteines and/or a E236A point-
698 mutation were introduced by PCR cloning involving QuikChange mutagenesis (Stratagene)
699 (Tomishige and Vale, 2000). For heterodimer, mutations were introduced into one of the
700 two polypeptide chains of the cysteine-light kinesin-1 heterodimer with 490 amino-acids
701 (Tomishige et al., 2006; Isojima et al., 2016). For single molecule fluorescent observation
702 of monomers, GFP (P64L/S65T variant) was fused at the C-terminal of constructs. All the
703 constructs were verified by DNA sequencing. Kinesin proteins were expressed and purified
704 as described previously (Tomishige and Vale, 2000; Tomishige et al., 2006) except that for
705 monomeric kinesins, Ni-NTA chromatography was followed by dialysis against 25 mM
706 PIPES (pH 7.0), 100 mM NaCl, 2 mM $MgCl_2$ and 100 μM ATP for 3 h at 4°C. EGTA in
707 the buffer was removed. For steady state ATPase assays and single molecule observations,
708 proteins were further purified with microtubule-affinity purification (Tomishige et al.,
709 2006). DTT and EGTA were removed from the solutions. Tubulin was purified and
710 polymerized as described previously (Woehlke et al., 1997). Protein concentrations were
711 determined by Bradford assays using BSA as a standard. For fluorescent labeling (smFRET
712 or mant-ATP binding measurement of heterodimer), dialyzed kinesin was reacted with
713 Cy3-maleimide (Cytiva), Cy5-maleimide (Cytiva), ATTO488-maleimide (ATTO-TEC) or
714 Alexa488-maleimide (Thermo Fisher). The labeled protein was further purified through
715 microtubule affinity purification as described (Yildiz et al., 2004; Tomishige et al., 2006).
716

717 **Chemical cross-linking**

718 Disulfide cross-link was formed by oxidation using copper and phenanthroline (Kobashi,
719 1968; Kaan et al., 2011). Reactions were carried out by addition of 10 μM $CuCl_2$ and 20
720 μM o-phenanthroline to 4 μM kinesin heads in 25 mM PIPES (pH 6.8) plus 2 mM $MgCl_2$
721 and incubation on ice for 3 h. The reactions were quenched by addition of 1 mM EGTA.
722 Control reactions were carried out in parallel by adding 10 mM DTT. Disulfide cross-

723 linking was verified using non-reducing SDS-PAGE with AMS (4'-acetamido-4'-
724 maleimidylstilbene-2,2'-disulfonic acid, 6508; Setareh Biotech) which react with reduced
725 cysteine residues causing band-shift on SDS-PAGE (Denoncin et al., 2013). Post cross-
726 linking reaction of kinesin (after addition of EGTA) was denatured by addition of 10%
727 trichloroacetic acid (TCA) and incubation for 30 min at 4°C. 100 µl of denatured kinesin
728 solution was centrifuged (100k rpm, for 5 min) and pellet was carefully washed with 50
729 mM Tris-HCl (pH 7.5) plus 10 mM EDTA to remove DTT or copper. The pellet was then
730 resuspended in 30 µl of solution containing 50 mM Tris-HCl (pH 7.5), 10 mM EDTA,
731 0.1% SDS, 20 mM AMS. The sample was incubated over night at room temperature under
732 shaking. Addition of SDS sample buffer without reducing reagents was followed by SDS-
733 PAGE (8.5% polyacrylamide) and CBB staining. Ratio of reduced and oxidized molecules
734 was quantified using ImageJ.
735
736 **Steady state ATPase assay**
737 Microtubule-stimulated ATPase activity was measured using spectrometer (V550; JACSO)
738 with a coupled enzymatic assay as described previously (Woehlke et al., 1997). The
739 ATPase assays were performed in BRB12 buffer (12 mM PIPES (pH 6.8), 2 mM $MgCl_2$, 1
740 mM EGTA) containing 1 mM ATP, 20 µM taxol, 0.1 mg/ml casein and coupled NADH
741 oxidation system (0.2 mM NADH, 5 mM phospho(enol)pyruvate, 10 µg/ml of pyrvate
742 kinase, and 10 µg/ml of lactate dehydrogenase). 1 mM DTT was also added when
743 measuring reducing conditions. The assays were started with 10 nM kinesin and varying
744 concentrations of microtubules at 22°C.
745
746 **Pre-steady state kinetics measurements**
747 All stopped flow experiments were performed at 25°C in BRB25 buffer (25 mM PIPES
748 (pH 6.8), 2 mM $MgCl_2$, 1 mM EGTA) using a KinTek Stopped flow system (SF2004;
749 Kintek Corp., State College, PA) with a Xenon lamp. Mant-nucleotide fluorescence
750 measurements were performed using an extension wavelength of 280 nm and fluorescence
751 emission was monitored using a 445/40 band pass filter (D445/40M; Chroma Tec). 5-10

752 fluorescent traces were averaged for each experimental condition. Turbidity measurements
753 were performed at 340 nm and 15-20 turbidity traces were averaged. Averaged stopped
754 flow traces were fit to single exponential function,

755 $$y = A\,exp(-k_{obs}t) + C \qquad \text{(Eq. 1)}$$

756 or a burst equation,

757 $$y = A\,exp(-k_{obs}t) + k_{ss}t + C \qquad \text{(Eq. 2)}$$

758 where k_{obs} is the rate constant of the initial exponential phase, k_{ss} is the rate constant of the
759 linear phase, A is the amplitude of exponential phase and C is the constant term.
760

761 **Mant-ATP binding kinetics**

762 Microtubule-kinesin complex was prepared by incubation of 3.2 μM post cross-linking
763 kinesin with 4 μM microtubule and 20 μM taxol in BRB25 buffer at room temperature for
764 10 min. Microtubule-C222/C334 kinesin complex was prepared by following procedure.
765 3.2 μM of reduced/oxidized C222/C334 kinesin was incubated with 4 μM microtubules, 20
766 μM taxol and 5 U/ml apyrase at room temperature for 1 h, followed by a centrifugation
767 (80k rpm, 10 min) on 20% sucrose cushion. For Alexa488-labeled heterodimer, 5 μM of
768 heterodimer kinesin was incubated with 25 μM microtubules in the presence of 1 mM ATP
769 at room temperature for 10 min, followed by a centrigugation (80k rpm, 10 min) on 60%
770 glycerol cushion. The pellet was resuspended in initial volume of BRB25 plus 20 μM taxol.
771 The concentration of the heterodimer-microtubule complex was estimated using the
772 extinction coefficient of Alexa488 dye (73,000 $cm^{-1}M^{-1}$) and was adjusted to approximately
773 1 μM after mixing. The microtubule-kinesin complex was then rapidly mixed with
774 increasing concentrations of mant-ATP (M12417; Invitrogen) or mant-dATP (3'-O-(N-
775 Methyl-anthraniloyl)-2'-deoxyadenosine-5'-triphosphate; Jena Bioscience). Fluorescence
776 data of mantATP binding were fit to single exponential (Eq. 1). Values of k_{obs} were plotted
777 against nucleotide concentration and fit to linear function,

778 $$k_{obs} = k_{+1}[\text{mantATP}] + k_{-1} \qquad \text{(Eq. 3)}$$

779 where k_{+1} is the second-order rate constant for nucleotide binding and k_{-1} is the rate
780 constant for nucleotide dissociation from the motor.

781

782 **Microtubule dissociation kinetics**

783 Microtubule-kinesin complex was prepared by incubation of 3.2 μM post cross-linking
784 kinesin with 4 μM microtubule, 20 μM taxol and 0.1 U/ml apyrase in BRB25 buffer at
785 room temperature for 10 min. 150 mM KCl was then added into kinesin solution. The
786 change in turbidity was monitored after rapid mixing of microtubule-kinesin complex with
787 ATP (1 mM post mixing) plus 150 mM KCl. Turbidity traces were fit to burst equation
788 (Eq. 2) to determine microtubule dissociation rate.

789

790 **Single molecule fluorescence observation of GFP-labeled kinesin**

791 Binding/detachment of individual GFP-fused kinesin on axonemes (purified from sea
792 urchin sperm flagella) were observed in a custom-build prism-type laser-illuminated total-
793 internal-reflection microscope as described (Tomishige and Vale, 2000). Assay chamber
794 constructed between a quartz slide and a coverslip was first filled with axonemes diluted in
795 BRB12 for 3min, followed by a washing with 1mg/ml casein in BRB12 for 3 min. The
796 chamber was then filled with the assay solution contained GFP-kinesin (200 pM for WT,
797 C47/C328 and C47/C335, 500 pM for C222/C334 and C4/C330), 1 mM ATP, 100 mM
798 KCl and oxygen scavenging system (4.5 mg/ml glucose, 50 U/ml catalase, 50 U/ml
799 glucose-oxidase) and sealed. 70 mM 2-mercaptoethanol was added in the assay solution
800 when observing in reducing condition. GFP molecules were exited at 488 nm and
801 fluorescence was recorded at 10 ms temporal resolution. Distributions of dwell time on
802 axonemes were obtained from kymographs. Fluorescent spots dwelled more than two
803 frames were used for analysis. Detachment rates were determined by single exponential
804 fitting of the dwell histograms.

805

806 **Flow-cell chamber preparation for single molecule FRET**

807 For the wild-type monomeric kinesin, flow-cell chamber was constructed between poly-L-
808 lysine-coated quartz slide and cover slip. The chamber was first filled with microtubule in
809 BRB12 buffer containing 20 μM taxol for 5 min. Then, BRB12 buffer containing 20 μM

taxol and 1 mg/ml casein was infused and incubated for 2 min followed by washing with BRB12 buffer containing 20 μM taxol. The chamber was finally filled with observation buffer containing an ATP regenerating system (10 μg/ml creatin kinase, 2 mM creatin phosphate), an oxygen scavenging system (2.5 mM protocatechuic acid (PCA), 1 unit/ml protocatechuate-3,4-dioxygenase (PCD) (P8279-25UN; Sigma), 2 mM Trolox) (Aitken et al., 2008), 150 mM KCl, 20 μM taxol, 500 nM Alexa Fluor 647 ATP (A22362; Invitrogen) and 100 pM kinesin in BRB12 buffer. All procedures were carried out at room temperature.

For the other constructs (E236A monomer, E236A-WT heterodimer), flow-cell chamber was constructed between quartz slide pre-cleaned with 0.1 M KOH and cover slip, separated by ~50 μm thickness. The cell was first filled with Protein A (Sigma P6031-1MG) solution (20 μl, 50 μg/ml) in BRB12 buffer (12 mM PIPES (pH 6.8), 2 mM $MgCl_2$, 1 mM EGTA) for 2 min. After washing unbound protein with 40 μl of BRB12 buffer, 20 μl of 20 μg/ml anti-α-tubulin antibody (Sigma T6199) solution in BRB12 buffer was infused for 5 min. Then unbound antibody was washed out with 40 μl of BRB12 buffer containing 20 μM taxol. Then, 40 μl of microtubule suspension in BRB12 buffer containing 20 μM taxol was infused and incubated for 2 min. Then, 40 μl of BRB12 buffer containing 20 μM taxol and 1 mg/ml casein was infused and incubated for 2 min. After washing with 40 μl of BRB12 buffer containing 20 μM taxol, the chamber was finally filled with observation buffer containing an ATP regenerating system (10 μg/ml creatin kinase, 2 mM creatin phosphate), an oxygen scavenging system (4.5 mg/ml glucose, 50 unit/ml glucose-oxidase, 50 unit/ml catalase, 0.5% 2-mercaptoethanol), 20 μM taxol, 200 nM Alexa Fluor 647 ATP (A22362; Invitrogen) and 100 pM kinesin in BRB12 buffer. All procedures were carried out at room temperature.

Single molecule FRET observation

Single molecule observation of fluorescently labeled kinesin was done under a prism-type total internal reflection fluorescence microscopy (Mori et al., 2007). We used ATTO 488 (WT monomer) and Cy3 (others) as a donor fluorophore. ATTO 488 was excited with 488 nm diode laser (Cyan-75-TA-FE; Spectra-Physics Inc.) and Cy3 was excited with 515 nm diode

839 laser (EXLSR-515-50-CDTF-E, Spectra-Physics Inc.). Fluorescent signals were collected
840 through objective lens and a specific filter for cutting of the excitation light and projected on
841 a cooled EMCCD camera. For smFRET observations, fluorescent signal was separated using
842 dichroic mirror and donor and acceptor fluorescence were simultaneously observed. Position
843 of microtubule was identified based on the fluorescence from the labeled kinesin. When more
844 than 5 fluorescent spots of donor fluorophore lied on a straight line, we assumed that these
845 spots were on the microtubule. FRET data were collected at 10 ms and 200 ms exposure
846 times for wild-type monomer and for E236A monomer and E236A-WT heterodimer,
847 respectively, at 22 °C. We identified ATP binding to the kinesin head when the FRET
848 efficiency exceeded a threshold of 0.5.
849
850 **Gold labeling of kinesin**
851 Purified kinesin was biotinylated, and biotinylated kinesin was bound to microtubules in the
852 presence of AMP-PNP as described previously (Isojima et al., 2016). Microtubule-bound
853 kinesin was then collected by centrifugation (230,000*g* for 10 min) and was immersed in
854 streptavidin solution containing 12 mM PIPES (pH6.8), 2 mM $MgCl_2$, 1 mM EGTA, 20 μM
855 taxol and 2.5 mg/ml streptavidin (191-12851; Wako Pure Chemical Industries) and incubated
856 20 min at room temperature. Microtubule-bound streptavidin-modified kinesin was collected
857 by centrifugation (230,000g for 10 min) and released from microtubules as described
858 previously. Biotin-coated gold nanoparticles were prepared as previously described (Isojima
859 et al., 2016), except that streptavidin was not added to the gold. Just before observation,
860 streptavidin-modified kinesin and biotin-coated gold nanoparticles were mixed at a 1:1
861 molecule/particle ratio.
862
863 **Total internal reflection dark-field microscopy**
864 A flow cell was constructed, and microtubules were attached on the glass surface by using
865 protein A and anti-α-tubulin antibody as described previously (Isojima et al., 2016). The cell
866 was then infused with 40 μl of BRB 12 buffer (12 mM PIPES (pH 6.8), 2 mM EGTA and 1
867 mM $MgCl_2$) containing 20 μM taxol and 1 mg/ml casein for 2 min. The cell was infused with

868 BRB12 buffer containing 3 nM gold-labeled kinesin for 5 min, and unbound kinesins and
869 gold nanoparticles were removed by washing with 60 μl of the BRB12 buffer containing 20
870 μM taxol. Finally, the flow cell was infused with 40 μl of the observation buffer (BRB12
871 buffer containing 70 mM β-mercaptoethanol, 10 μg/ml creatine kinase, 2 mM creatine
872 phosphate, 20 mM KCl and 1-1000 μM ATP), sealed with nail polish and used for
873 observation. All procedures were carried out at room temperature. The gold-labeled kinesin
874 was observed using a total internal reflection dark-field microscope as described previously
875 (Isojima et al., 2016) and the scattering images were recorded with a high-speed CMOS
876 camera (FASTCAM Mini AX100; Photron) at a frame rate of 20,000 fps (50 μs temporal
877 resolution). Observations were carried out at 24-26°C.
878
879 **Data analysis for the dark-field observations**
880 The coordinates of gold nanoparticles were determined as described previously (Isojima et
881 al., 2016). The orientations of the microtubule 'on axis' (orientation parallel to the
882 microtubule long axis) and 'off axis' (orientation perpendicular to the microtubule long axis)
883 were then determined from the aligned gold-labeled kinesin along the microtubule and
884 adjusted to X and Y coordinates as described previously. The 'bound' and 'unbound' states
885 of gold-labeled kinesin heads were determined as follows: two-dimensional standard
886 deviation (s.d.) of the trajectory for each time frame t was calculated as [t - 20, t + 20] and
887 the median μ and s.d. σ of the s.d. of the trajectory was determined by fitting the histogram
888 of the s.d. with a Gaussian function. Transitions from the bound to unbound state were
889 detected when the s.d. was higher than μ+4σ in 10 consecutive frames and transition from
890 the unbound to bound state were detected when the s.d. was lower than μ+4σ in 10
891 consecutive frames. The accurate frame of the transition was determined by fitting the on-
892 and off-axis trajectory near the transition with two state step function. In the case of G0
893 construct, if two unbound states were closer than 50 ms and on-axis average of the bound
894 state between these unbound states was separated from the other bound states, these unbound
895 states and bound state were determined as unbound state 1-3 (**Figure 4–figure supplement**
896 **2**). The rate constants of each state were determined by fitting the histogram of the dwell time

with single exponential functions.

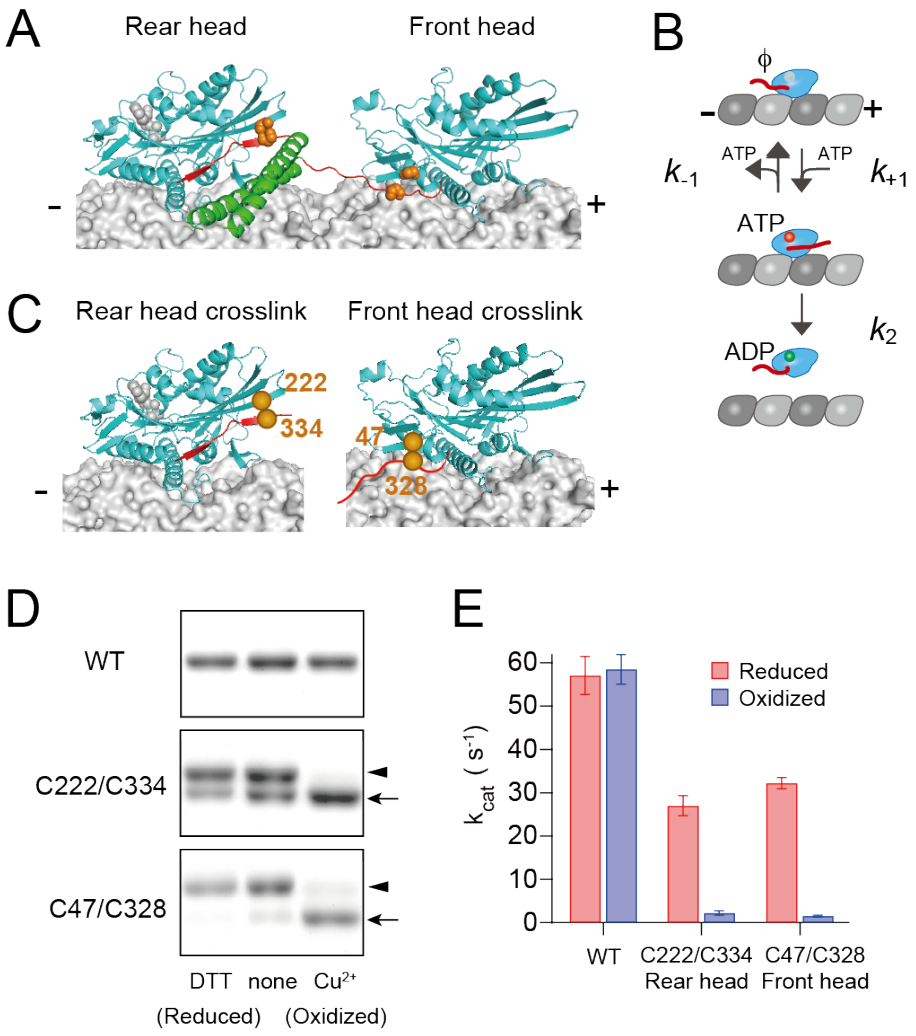

Figure 1. Disulfide-crosslinking to constraint the neck linker in either the forward or backward pointing configuration. (**A**) Three-dimensional structure of kinesin dimer on the microtubule in the two-head-bound intermediate state (modeled based on PDB# 4HNA and 4LNU). The motor domain, neck linker, and neck coiled-coil are shown in cyan, red, and green. Orange spheres represent the positions of cysteine residues as described in panel **C**. (**B**) Michaelis-Menten kinetics scheme for ATP-promoted dissociation of kinesin head from the microtubule, which includes ATP-binding (k_{+1}), ATP-dissociation (k_{-1}), and ATP-induced microtubule-dissociation (k_2) steps. (**C**) Positions of the cysteine residues for disulfide-crosslinking of monomeric kinesin. Cys222 and Cys334 were introduced to constrain the neck linker in the forward, docked conformation (left), while Cys47 and Cys328 were introduced to constrain the neck linker in the backward-pointing configuration (right). (**D**) Disulfide crosslinking after oxidative treatment was analyzed by nonreducing SDS-PAGE. WT (without Cys introduction), C222/C334, and C47/C328 constructs were treated with a reducing reagent (DTT), none, or oxidizing reagents (Cu^{2+}). Arrows and arrowheads indicate

un-crosslinked and intramolecular crosslinked kinesins, respectively. The whole image of the gels is shown in **Figure 1–figure supplement 1**. (**E**) Microtubule-activated ATPase under reduced and oxidized conditions. k_{cat} and K_m(MT) were determined from the fit to a Michaelis-Menten equation of ATP turnover rates at various microtubule concentrations (**Figure 1–figure supplement 2**). Mean ± s.e.m. values were obtained from three independent assays.

Figure supplement 1. Estimation of disulfide-crosslinking efficiency.

Figure supplement 2. Steady-state microtubule-activated ATPase rates of monomeric kinesins before and after oxidative crosslinking.

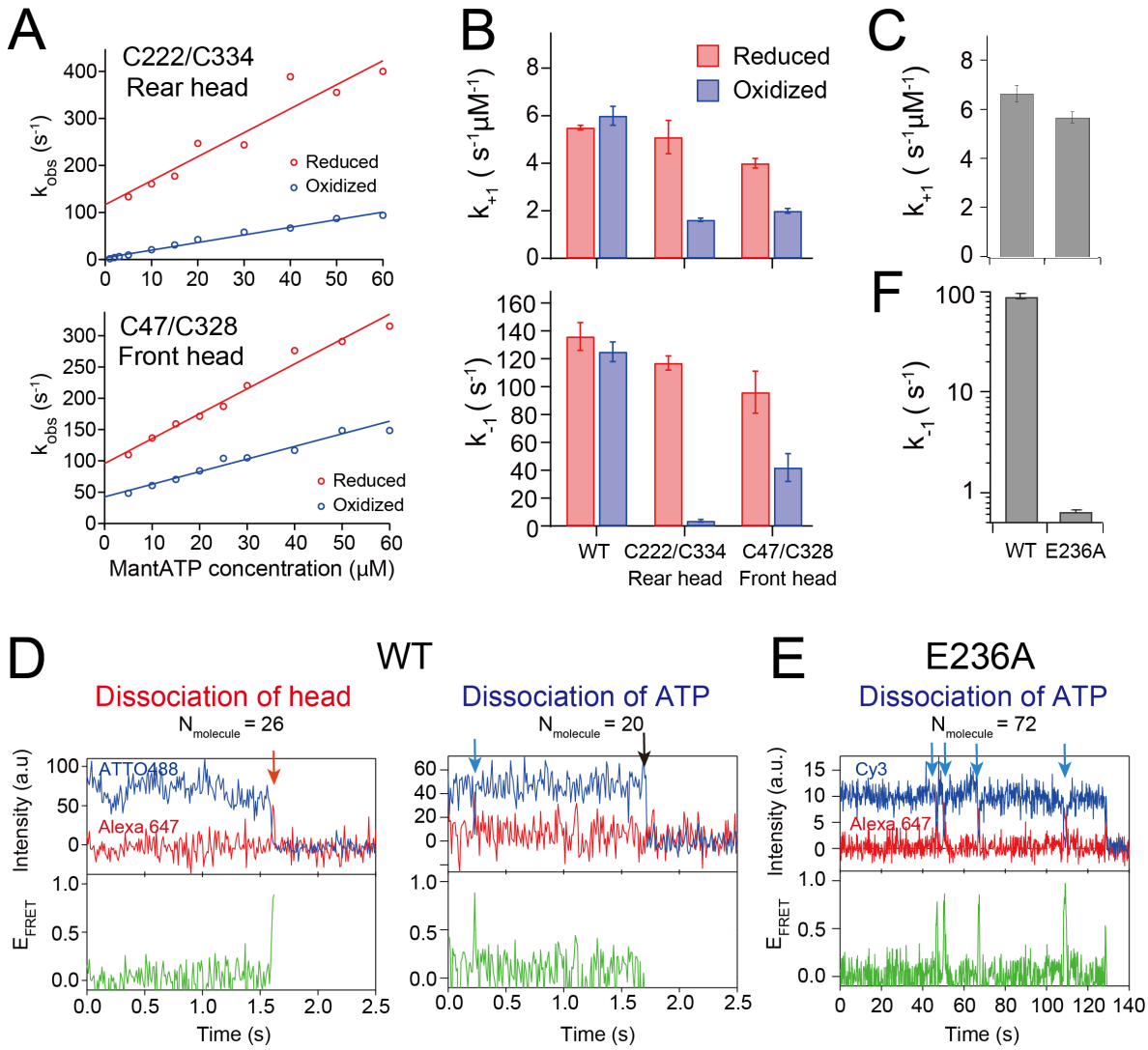

Figure 2. ATP-binding/dissociation kinetics of disulfide-crosslinked monomers. (**A**) The rate of initial enhancement of the fluorescence after rapid mixing of kinesin-microtubule complex with mant-ATP (k_{obs}; **Figure 2–figure supplement 1**) was plotted as a function of mant-ATP concentration. Solid lines represent a linear fit; the slope provides the on-rate of mant-ATP (k_{+1}) and the off-set provides the off-rate of mant-ATP (k_{-1}). (**B**) ATP binding rate k_{+1} and ATP dissociation rate k_{-1} of monomers before and after crosslinking obtained from the fit shown in pane **A**. Error bar shows the fit error. (**C**) Mant-dATP binding rate k_{+1} to wild-type (WT) and E236A monomers (k_{obs} plots are shown in **Figure 2–figure supplement 2**). (**D**) Two typical traces of smFRET between the donor-labeled wild-type monomer and Alexa-ATP (500 nM). Fluorescence intensities of donor (blue) and acceptor (red), and the calculated FRET efficiency (green) recorded at 100 fps are shown. Left trace: the FRET efficiency transiently increases just before both dyes disappear (indicated by the red arrow), suggesting that the nucleotide-bound head detached from the microtubule

(**Figure 2–figure supplement 4A**). Right trace: the FRET efficiency transiently increases, followed by the recovery of donor fluorescent (shown by the blue arrow), indicating the reversible dissociation of ATP. The black arrow indicates the photobleaching of the donor dye. The numbers of molecules observed for each type is shown at the top of the traces. (**E**) Typical trace of smFRET between the E236A monomer and Alexa-ATP (200 nM) recorded at 5 fps, demonstrating repetitive ATP binding and dissociation. (**F**) The dissociation rate k_{-1} of Alexa-ATP from wild-type and E236A monomers (histograms are shown in **Figure 2–figure supplement 4B**). The value for the wild-type may be underestimated due to the limited temporal resolution (10 ms).

Figure supplement 1. Pre-steady-state kinetics of ATP binding to monomeric kinesin-microtubule complex before and after crosslinking.

Figure supplement 2. ATP binding kinetics for E236A mutant monomer on microtubule.

Figure supplement 3. Processive motility of wild-type kinesin dimer driven by Alexa 647 ATP.

Figure supplement 4. Dwell time of Alexa-ATP-bound state for wild-type and E236A monomers determined using smFRET.

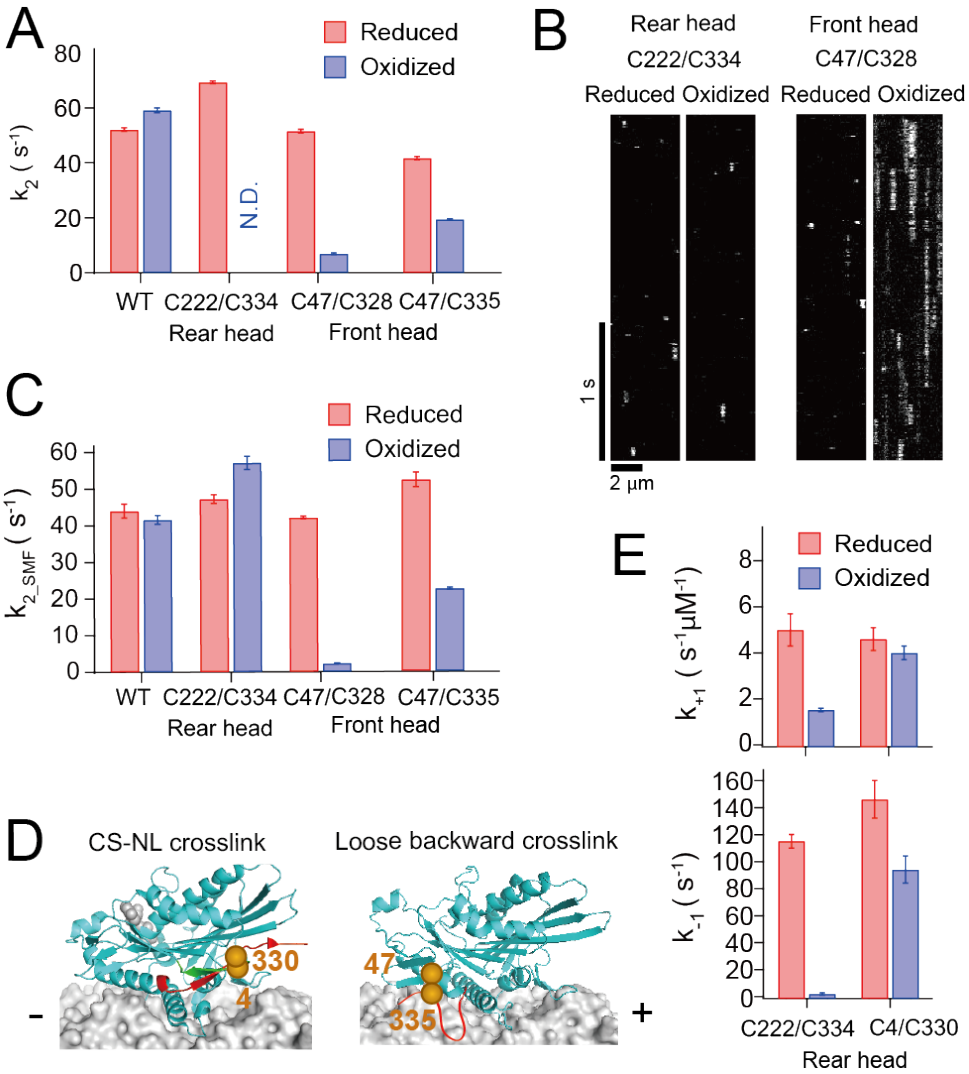

Figure 3. Microtubule-detachment kinetics of disulfide-crosslinked monomers. (**A**) ATP-induced dissociation rate from microtubule k_2 measured by turbidity change after the rapid mixing of kinesin-microtubule complex with 1 mM ATP. The turbidity time traces are shown in **Figure 3–figure supplement 1**. (**B**) Kymographs showing the binding and dissociation of GFP-fused kinesin under reduced and oxidized conditions on the microtubule. C47/C328 showed an extended dwell on the microtubule after crosslinking. (**C**) ATP-induced dissociation rate from the microtubule measured using single-molecule observations of GFP-fused kinesin. k_{2_SMF} was determined as an inverse of the mean dwell time of the fluorescent kinesin on the microtubule in the presence of 1 mM ATP. The dwell time histograms are shown in **Figure 3–figure supplement 2B**. (**D**) Positions of Cys4 and Cys330 residues for disulfide-crosslinking of a monomer between the N-terminal cover strand (CS; green) and the neck linker (NL; red) (left). Positions of Cys47 and Cys335 residues for disulfide-crosslinking of a monomer to constrain the neck linker in the backward-pointing configuration allowing partial docking of the neck linker (right; **Figure**

3−figure supplement 3). The ATP-induced dissociation rates from the microtubule of C47/C335 monomer before and after crosslinking, measured by turbidity change (k_2) and single-molecule fluorescence (k_{2_SMF}), are shown in **Figure 3A, C**. Histograms are displayed in **Figure 3−figure supplement 4E**. (**E**) Mant-ATP binding rate k_{+1} and dissociation rate k_{-1} of C4/C330 monomer before and after crosslinking (data for C222/C334 are included from **Figure 2B** for comparison). The k_{obs} plots are shown in **Figure 3−figure supplement 4B**.

Figure supplement 1. ATP-induced dissociation kinetics of crosslinked kinesin from microtubule measured using light scattering.

Figure supplement 2. ATP-dependent microtubule-binding and -dissociation of crosslinked kinesins observed by single-molecule fluorescence microscopy.

Figure supplement 3. Locations of the C47/C328 and C47/C335 residues when the labeled head is in the front or rear of dimeric kinesin.

Figure supplement 4. Kinetics measurements of ATP-binding and microtubule-dissociation of C4/C330 and C47/C335 crosslinked monomeric kinesins.

			Rear head		Front head	
	WT		C222/C334		C47/C328	
	Reduced	Oxidized	Reduced	Oxidized	Reduced	Oxidized
k_{cat} (s^{-1})	57.1 ± 4.4	58.5 ± 3.4	27.0 ± 2.3	2.2 ± 0.5	32.2 ± 1.3	1.5 ± 0.2
K_m(MT) (μM)	0.31 ± 0.08	0.36 ± 0.08	0.23 ± 0.06	0.200 ± 0.007	0.28 ± 0.06	0.13 ± 0.04
k_{+1} ($s^{-1}\mu M^{-1}$)	5.5 ± 0.1	6.0 ± 0.4	5.1 ± 0.7	1.62 ± 0.07	4.0 ± 0.2	2.0 ± 0.1
k_{-1} (s^{-1})	136 ± 5	125 ± 12	117 ± 23	3.7 ± 1.9	96 ± 6	42 ± 4
k_2 (s^{-1})	52.1 ± 0.6	59.1 ± 0.9	69.3 ± 0.5	N.D.	51.5 ± 0.7	7.0 ± 0.3
k_{2_SMF} (s^{-1})	44.0 ± 1.9	41.6 ± 1.2	47.2 ± 1.2	57.1 ± 2.3	42.1 ± 0.4	2.30 ± 0.08

	C4/C330		C47/C335	
	Reduced	Oxidized	Reduced	Oxidized
k_{cat} (s^{-1})	33.5 ± 2.1	32.6 ± 1.2	43.1 ± 3.0	11.9 ± 0.6
K_m(MT) (μM)	0.42 ± 0.08	8.36 ± 0.98	0.33 ± 0.05	0.10 ± 0.01
k_{+1} ($s^{-1}\mu M^{-1}$)	4.7 ± 0.5	4.1 ± 0.3	9.1 ± 0.3	4.5 ± 0.1
k_{-1} (s^{-1})	148 ± 18	96 ± 9	85 ± 10	41 ± 5
k_2 (s^{-1})	68.6 ± 0.5	80.8 ± 0.8	41.6 ± 0.6	19.4 ± 0.2
k_{2_SMF} (s^{-1})	59.5 ± 2.3	58.4 ± 2.6	52.1 ± 2.0	22.5 ± 0.3

Table 1. Kinetic rate constants for disulfide-crosslinking monomers. Steady-state ATP-turnover rate (k_{cat} and K_m(MT)), pre-steady-state mant-ATP binding (k_{+1} and k_{-1}) and microtubule dissociation rates (k_2 and k_{2_SMF}, measured by light scattering and single-molecule fluorescence) measured under reduced and oxidized conditions.

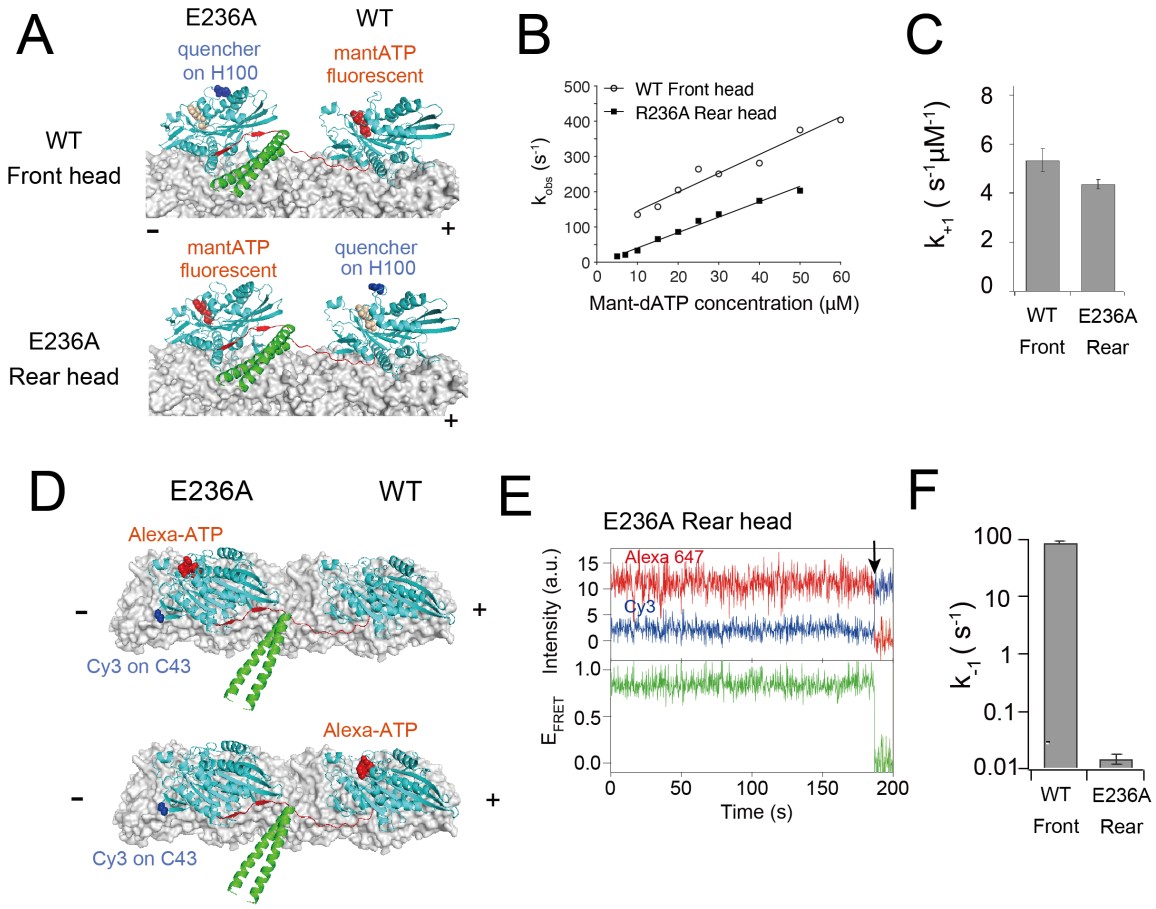

Figure 4. ATP-binding/dissociation kinetics of the E236A-WT heterodimer. (**A**) Diagram showing the positions of H100 residue (highlighted in blue) labeled with Alexa 488 dye. This label quenches the mant-ATP signal of either the rear W236A head (upper; used to measure ATP-binding to the front head) or the front wild-type head (lower; used to measure ATP-binding to the rear head). (**B**) k_{obs} plots for mant-ATP binding to the front wild-type and rear E236A heads of the E236A-WT heterodimer (typical fluorescent transients are shown in **Figure 4–figure supplement 2**). Solid lines indicate a linear fit. The fit parameters are k_{+1} = 5.3 ± 0.5 $\mu M^{-1}s^{-1}$ and k_{-1} = 92 ± 16 s^{-1} for WT front head and k_{+1} = 4.4 ± 0.2 $\mu M^{-1}s^{-1}$ and k_{-1} = −3.3 ± 5.1 s^{-1} for E236A rear head. (**C**) ATP-binding rate (k_{+1}) for front and rear heads of the E236A-WT heterodimer, as determined by fitting in panel **B**. (**D**) Diagram showing the position of Cys43 residue of E236A chain for labeling with donor (Cy3; blue) fluorophore, and the Alexa 647 ATP (red) bound to the rear E236A head (upper) or the front wild-type head (lower) of the E236A-WT heterodimer. High FRET efficiency is expected when the Alexa-ATP binds specifically to the rear E236A head. (**E**) A representative trace of fluorescence intensities of donor (Cy3; blue) on the E236A rear head and acceptor (Alexa 647; red) fluorophores, with calculated FRET efficiency (green), for the E236A-WT heterodimer at 200 nM Alexa-ATP recorded at 5 fps. The black arrow

indicates the dissociation of Alexa-ATP, accompanied by the recovery of donor fluorescent. ATP remained bound to the rear head significantly longer compared to the E236A monomer (**Figure 2E**). (**F**) ATP dissociation rate (k_{-1}) for front and rear heads of the E236A-WT heterodimer. Note that these rates were measured using different methods (stopped flow for the WT font head (**Figure 4B**) and smFRET for the E236A rear head (**Figure 4E**)) and thus cannot be directly compared.

Figure supplement 1. Single-molecule FRET between two heads of E236A-WT heterodimer.

Figure supplement 2. ATP binding kinetics for front and rear heads of E236A-WT heterodimer.

Figure supplement 3. Single-molecule FRET observation between donor dye on one of the head of E236A-WT heterodimer and acceptor-labeled ATP.

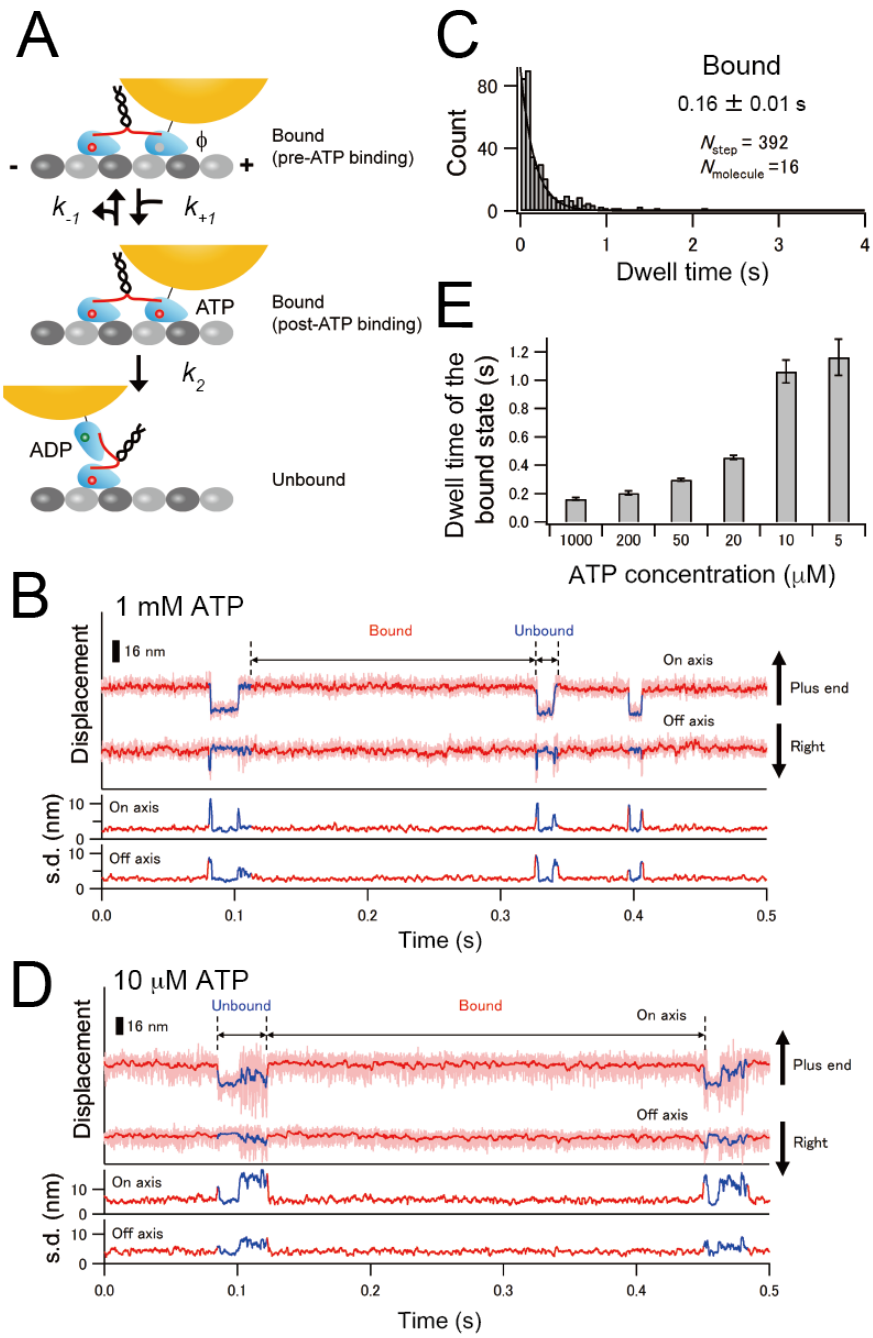

Figure 5. Microtubule-detachment kinetics of the front WT head of E236A-WT heterodimer. (**A**) A diagram illustrating the kinetic transitions for the detachment of the gold-labeled WT head of the E236A-WT heterodimer. Upon binding to the microtubule, the front head releases ADP, becoming a nucleotide-free state (indicated as ϕ; pre-ATP binding). The detachment kinetics from this state can be described using the same scheme as the monomer (**Figure 1B**). (**B**) Typical trace for the centroid positions of the gold probe attached to the WT head of the E236A-WT heterodimer in the presence of 1 mM ATP (light red lines), toward the microtubule long axis (on axis) and perpendicular to the microtubule

axis (off axis). Red and blue lines depict the median-filtered trace (with a window size of 51 frames) for the bound and unbound states, respectively. Lower panels display the standard deviation (s.d.) of on- and off-axis positions for each time frame t (calculated as [t – 20, t + 20]). (**C**) Histogram of the dwell time in the bound state. The solid line shows the fit with an exponential function. The number represents the average dwell time (± s.e.m.) determined from the fit. (**D**) Typical trace for the centroid positions of the gold probe attached to the WT head of E236A-WT heterodimer in the presence of 10 μM ATP. (**E**) Mean dwell times in the bound state under various ATP concentrations as determined from the fit of the histograms of the dwell times (**Figure 5-figure supplement 3**).

Figure supplement 1. Long-term trace of the gold-labeled E236A-WT heterodimer exhibiting very slow stepping motion.

Figure supplement 2. The unbound state of the gold-labeled WT head of the E236A-WT heterodimer.

Figure supplement 3. Distributions of the dwell time in the bound and unbound states of the leading WT head of E236A-WT heterodimer.

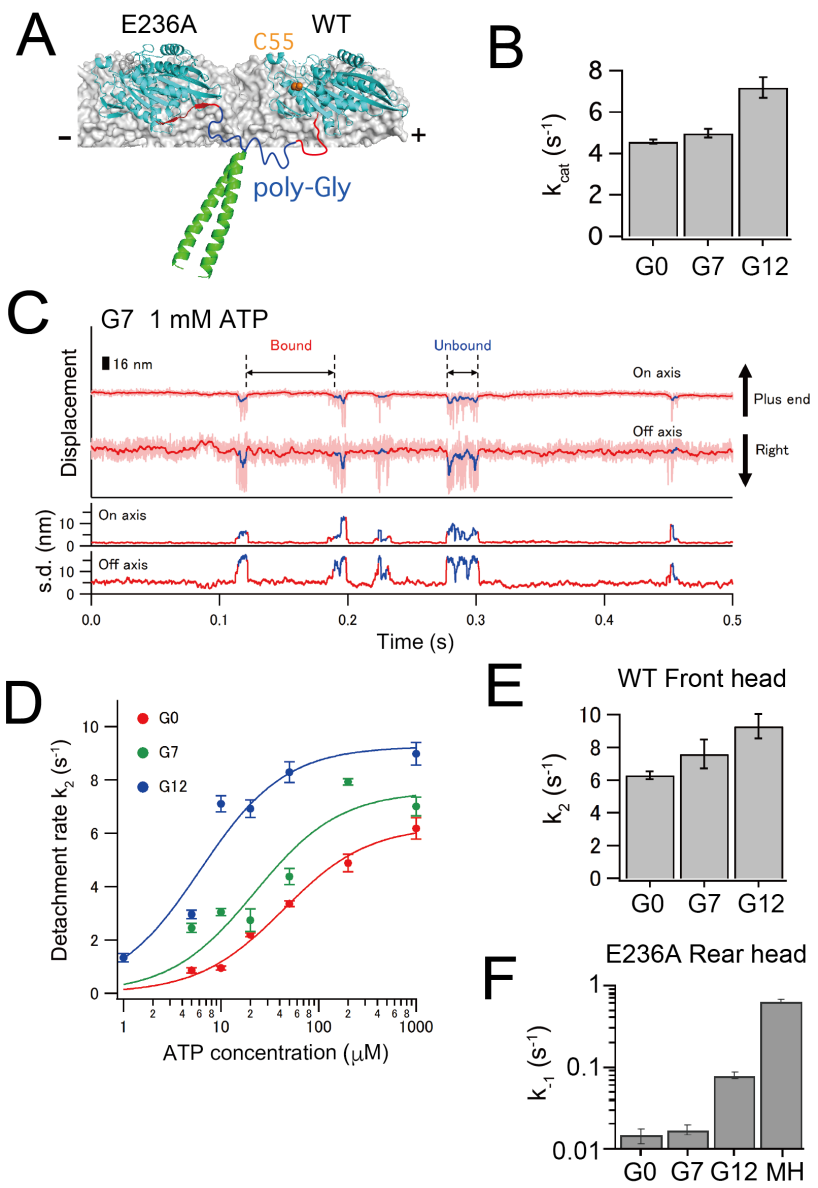

Figure 6. Effect of the tension applied to the neck linker on the gating examined using the neck-linker extended E236A-WT heterodimer. (**A**) Diagram showing the position of the poly-Gly residues (blue) inserted between the neck linker (red) and the neck coiled-coil (green). The Cys55 residue for gold-labeling is represented by an orange sphere. (**B**) k_{cat} for the microtubule-activated ATPase of E236A-WT heterodimers without (termed as G0) and with neck-linker extensions (G7 and G12) (**Figure 6-figure supplement 1**). (**C**) Typical trace for the centroid positions of the gold probe attached to the WT head of the E236A-WT heterodimer with a 7 poly-Gly insertion in the presence of 1 mM ATP. (**D**) The inverse of the mean dwell time in the bound state was plotted as a function of ATP concentration, as determined from the fit of the histograms of the dwell times (**Figure 6-figure supplement 2, 3**). Error bars represent s.e.m. The solid lines show the fit with the Michaelis-Menten

equation. The fit parameters are k_{cat} (or k_2) = 6.3 ± 0.2 s^{-1} and K_m (ATP) = 43 ± 6 μM for G0, k_{cat} = 7.0 ± 0.5 s^{-1} and K_m (ATP) = 12 ± 3 μM for G7, and k_{cat} = 9.3 ± 0.7 s^{-1} and K_m (ATP) = 6.1 ± 2.1 μM for G12. The K_m (ATP) decreases as the insertion length increases. (**E**) The k_{cat} value, which represents the ATP-induced detachment rate of the front head k_2, obtained from the fit shown in panel **d**. The error bars represent s.e.m. (**F**) The ATP dissociation rates k_{-1} for the E236A rear head of the wild-type (G0), G7 and G12 E236A-WT heterodimer were determined using smFRET. The k_{-1} was calculated as the inverse of the mean dwell time for the high FRET state (see the typical trace and dwell time histograms for the G7 and G12 heterodimer in **Figure 6-figure supplement 5**). For comparison, data for the E236A monomer head (referred to as MH) is included from **Figure 2F**.

Figure supplement 1. Microtubule-activated ATPase rates of the E236A-WT heterodimer with and without neck-linker extension.

Figure supplement 2. Distributions of the dwell time in the bound and unbound states of the leading WT head of E236A-WT heterodimer with 7 poly-Gly insertion (G7).

Figure supplement 3. Distributions of the dwell time in the bound and unbound states of the leading WT head of E236A-WT heterodimer with 12 poly-Gly insertion (G12).

Figure supplement 4. Binding to the rear-tubulin binding site observed for the G12 E236-WT heterodimer.

Figure supplement 5. Single molecule FRET between donor-labeled E236A head of E236A-WT heterodimer with extended neck linker and acceptor-conjugated ATP.

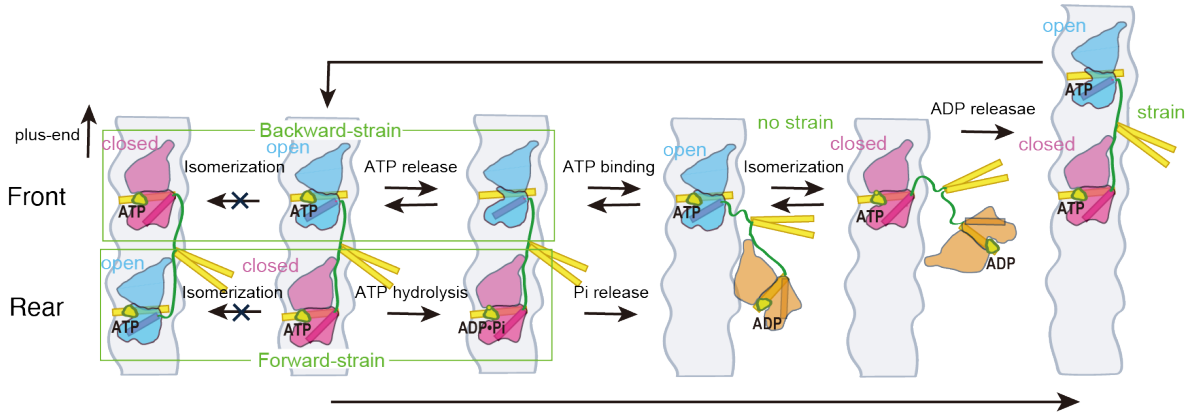

Figure 7. Model to explain how the tension exerted by the stretched neck linker in dimeric kinesin coordinates the microtubule detachment of the two heads. This model is based on the proposal that the transition between ATP-bound open and closed conformations of the head is regulated by the neck linker strain (**Figure 7-figure supplement 2**). The open and closed conformational states of the head are indicated in blue and red, respectively, with the α6 helix, which connects to the neck linker, highlighted as a rod. The microtubule-detached ADP-bound state is shown in orange. The neck linker is depicted in green, while the α4 helix, which directly interacts with the microtubule, and the neck coiled-coil are shown in yellow. In the two-head-bound state, the front head remains in the open state because the backward strain prevents it from transitioning to the closed state. In this state, ATP can weakly bind to the nucleotide-pocket but often dissociates. Conversely, the rear head is stabilized in the closed state because the transition to the open state is suppressed by the forward strain. ATP is tightly bound to the closed nucleotide-pocket, causing the rear head to hydrolyze ATP and detach from the microtubule before the front head does. In the one-head-bound state, the microtubule-bound head can transition between the open and closed states. However, once the tethered head binds preferentially to the forward tubulin-binding site, the strain built up between the two microtubule-bound heads stabilizes the rear head in the closed conformation and the front head in the open conformation.

Figure supplement 1. Structural difference between the open and closed conformational states of the kinesin head.

Figure supplement 2. Schematic model showing that the open-closed conformational transition (isomerization) is gated by the neck linker strain.